Atmos. Chem. Phys. Discuss., 11, 13525–13574, 2011
www.atmos-chem-phys-discuss.net/11/13525/2011/
doi:10.5194/acpd-11-13525-2011

Atmospheric Chemistry and Physics Discussions

Airborne DOAS measurements in Arctic: vertical distributions of aerosol extinction coefficient and NO_2 concentration

A. Merlaud[1], M. Van Roozendael[1], N. Theys[1], C. Fayt[1], C. Hermans[1], B. Quennehen[2], A. Schwarzenboeck[2], G. Ancellet[3], M. Pommier[3], J. Pelon[3], J. Burkhart[4], A. Stohl[4], and M. De Mazière[1]

[1]Belgian Insitute for Space Aeronomy (BIRA-IASB), Avenue Circulaire 3, 1180 Brussels, Belgium
[2]Laboratoire de Météorologie Physique, Université B. Pascal, CNRS, France
[3]UPMC Univ. Paris 06; Université Versailles St-Quentin; CNRS/INSU, UMR 8190, LATMOS-IPSL, Paris, France
[4]Norwegian Institute for Air Research (NILU), Instituttveien 18, NO-2007 Kjeller, Norway

Received: 25 February 2011 – Accepted: 18 April 2011 – Published: 4 May 2011

Correspondence to: A. Merlaud (alexis.merlaud@aeronomie.be)

Published by Copernicus Publications on behalf of the European Geosciences Union.

Abstract

We report airborne differential optical absorption spectroscopy (DOAS) measurements of aerosol extinction and NO_2 tropospheric profiles performed off the North coast of Norway in April 2008. The DOAS instrument was installed on the Safire ATR-42 aircraft during the POLARCAT-France spring campaign and recorded scattered light spectra in near-limb geometry using a scanning telescope. We use O_4 slant column measurements to derive the aerosol extinction at 360 nm. Regularization is based on the maximum a posteriori solution, for which we compare a linear and a logarithmic approach. The latter inherently constrains the solution to positive values and yields aerosol extinction profiles more consistent with independently measured size distributions. Two soundings are presented, performed on 8 April 2008 above 71° N, 22° E and on 9 April 2008 above 70° N, 17.8° E. The first profile shows aerosol extinction and NO_2 in the marine boundary layer with respective values of $0.04 \pm 0.005\,km^{-1}$ and $1.9 \pm 0.3 \times 10^9\,molec\,cm^{-3}$. A second extinction layer of $0.01 \pm 0.003\,km^{-1}$ is found at 4 km altitude. During the second sounding, clouds prevented us to retrieve profile parts under 3 km altitude but a layer with enhanced extinction ($0.025 \pm 0.005\,km^{-1}$) and NO_2 ($1.95 \pm 0.2 \times 10^9\,molec\,cm^{-3}$) is clearly detected at 4 km altitude.

From CO and ozone in-situ measurements complemented by back-trajectories, we interpret the measurements in the free troposphere as, for the first sounding, a mix between stratospheric and polluted air from Northern Europe and for the second sounding, polluted air from Central Europe containing NO_2. Considering the boundary layer measurements of the first flight, modeled source regions indicate closer sources, especially the Kola Peninsula smelters, which can explain the NO_2 enhancement not correlated with a CO increase at the same altitude.

ACPD
11, 13525–13574, 2011

1 Introduction

Despite its remoteness, the Arctic troposphere is affected by trace gases and aerosols emissions from mid-latitude regions. The Arctic Haze phenomenon, observed since the 1950s, is a visible manifestation of this long-range transport (Shaw, 1995). The effects of this pollution are specific to the area and may explain part of the enhanced warming observed there. Indeed, the dry arctic air makes the area more sensitive to non-water-vapor greenhouse gases. Furthermore, above the high-albedo snow and ice surfaces, aerosols – even if only weakly absorbing – can lead to a warming, contrary to their global cooling effect (Law and Stohl, 2007, and references therein). Climate change may further modify the arctic tropospheric composition. For instance, if the summer sea ice continues its decline, ship traffic through the Northern passages will become an important source for aerosol and NO_x, the latter also driving an increase in tropospheric ozone (Granier et al., 2006). Quantifying such phenomena requires an accurate knowledge of the Arctic troposphere. In this paper we present airborne DOAS measurements of the vertical distribution of aerosol extinction coefficient and NO_2 concentration off the North coast of Norway during the POLARCAT-France spring campaign.

Differential Optical Absorption Spectroscopy (DOAS) has been widely used for atmospheric research (Platt and Stutz, 2008). First applied to the retrieval of stratospheric gas columns using zenith-sky observations of solar scattered light, the technique has been recently extended to the detection of tropospheric gases by means of observations along multiple viewing directions (Multi-Axis DOAS; Hönninger et al., 2004). Such measurements also yield information on the vertical distribution of the gases (Wittrock et al., 2004). The possibility to extend this profiling technique to aerosol extinction was demonstrated (Wagner et al., 2004; Friess et al., 2006) and implemented by several groups (Irie et al., 2008; Clémer et al., 2010). The approach uses the $(O_2)_2$ collision complex, referred hereafter as O_4, which presents strong absorption bands in the UV-Visible range. Aerosols affect DOAS measurements of any absorber by modifying the

ACPD
11, 13525–13574, 2011

light path but the effect can be isolated for O_4 since its vertical distribution is well-known. The vertical resolution achieved from ground remains however poor, typically two independent layers can be retrieved close to the surface and only little information in the free troposphere. Likewise, satellite-borne DOAS instruments, as the Ozone Monitoring Instrument (OMI, Levelt et al., 2006) are only sensible to the total tropospheric column. A way to overcome this limitation relies in operating a DOAS instrument from aircraft, combining the multi-axis measurements at different altitudes. The Airborne Multi-Axis DOAS (AMAXDOAS) instrument, recording simultaneously scattered-light spectra at different angles from an airplane, has already measured NO_2 vertical distributions (Bruns et al., 2006) in a polluted region. Prados-Roman et al. (2010) have used another airborne set-up with a single line-of-sight, parallel to the plane's ground and derived BrO Arctic profiles from the ascent of the aircraft. The instrument developed in this work, namely the Airborne Limb Scanning DOAS (ALS-DOAS), combines the two set-ups with a single line-of-sight scanning the horizon continuously.

In the next section we describe the technical aspects of the ALS-DOAS instrument and its operation on the Safire ATR-42 during the POLARCAT-France spring campaign. The methods used for the data analysis, i.e. the DOAS settings, radiative transfer modeling, inversion schemes and error budget are presented in Sect. 3. These methods are applied in Sect. 4 to two soundings performed during the flights on 8 and 9 April 2008. Retrieved extinctions are compared with Mie-scattering calculations performed on aerosol size distributions measured in situ. In Sect. 5, we interpret these results using ancillary measurements of CO and ozone mixing ratios, as well as backward trajectories calculations.

ACPD
11, 13525–13574, 2011

2 The ALS-DOAS instrument and its operation during a POLARCAT campaign

2.1 Instrumental description

The Airborne Limb Scanning DOAS (ALS-DOAS) was developed at the Belgian Institute for Space Aeronomy (BIRA-IASB) and first used during the POLARCAT campaign. Based on a grating spectrometer, it records limb-scattered sky light spectra at several angles around the horizon, following the Multi-axis DOAS principle (Hönninger et al., 2004).

Figure 1 shows the ALS-DOAS installed in the SAFIRE ATR-42 aircraft. The entrance optic is composed of a 1° field-of-view telescope focusing the light into an optical fiber. A 5-cm black paperboard baffle limits the stray light at the entrance of the telescope. This telescope, standing behind a BK-7 glass port, is mounted on a stepper-motor axis and is continuously scanning between −5° and 5° by steps of 1°. Between the fiber and the spectrometer, a Jobin Yvon optical interface matches the fiber and spectrometer numerical apertures. The spectrometer is a SpectraPro-150 (imaging Czerny-Turner set-up, 150 mm focal length) from Acton Research Corporation, with a 100 microns entrance slit. The spectral range is 330–450 nm, with a resolution of 0.4 nm full width at half maximum (UV) to 0.6 nm (visible). A custom Terimide 7 thermal insulation limits the thermal effects on the spectrometer and the matching interface. The detector, a back-illuminated Pixis CCD 2048*512 from Princeton Instruments, is cooled at −50 °C to increase the signal-to-noise ratio on the spectra. The whole set-up including the computer is mounted on a 19′ rack. While measuring, the CCD integration time is automatically adjusted to optimize the signal, typically between 0.4 and 1.3 s. Each measurement represents a 30 s average at a certain telescope angle, the latter is changed after each completed record. The acquisition is controlled automatically and the instrument does not need an operator onboard.

Several tropospheric molecules absorb light in the spectral range of our instrument and thus are potentially detectable: O_3, NO_2, HCHO, CHOCHO, O_4, IO and BrO. In the

ACPD
11, 13525–13574, 2011

following, we focus on O_4 and NO_2 measurements which were most clearly identified during the campaign.

2.2 The POLARCAT-France spring campaign

The POLARCAT-France spring campaign was part of the POLARCAT international research activity (Polar Study using Aircraft, Remote Sensing, Surface Measurements and Models, of Climate, Chemistry, Aerosols, and Transport), in the framework of the International Polar Year (IPY). Based in Kiruna, Sweden (68° N, 20° E), the Safire ATR-42 aircraft performed twelve scientific flights between continental Norway and Svalbard between 30 March and 11 April 2008. Scientific objectives of the campaign included the study of pollution transport, aerosol/cloud interactions and satellite validation. Various flight patterns were achieved in different weather conditions to fulfill these different research requirements. The aircraft's payload included remote sensing (e.g. Lidar, Radar) and in situ instruments (e.g. aerosol sampler, cloud particle imager). In Sect. 4, the aerosol size distributions measured by the Scanning Mobility Particle Sizer (SMPS, Villani et al., 2008) and by the Passive Cavity Aerosol Spectrometer Probe (PCASP 100-X DMT) aboard the Safire ATR-42 are used to calculate aerosol extinctions and compare with our retrievals. Together the instruments cover the size range between 0.02 and 3 microns. In Sect. 5 we also present ozone and CO profiles from the MOZART instrument (Nedelec et al., 2003; Ancellet et al., 2009) and attenuated backscatter ratio profiles at 532 nm and 1062 nm measured with the Lidar as described in de Villiers et al. (2010).

The ALS-DOAS instrument recorded spectra continuously during the campaign, except during the flight as0829 (7 April 2008) due to a computer problem. Here we focus on the data collected during two soundings on 8 (flight as0831) and 9 April 2008 (flight as0833), respectively above 71° N, 22° E and 70° N, 17.8° E. Figure 2 displays these flight tracks and the position of the soundings. During the first sounding, the plane was first flying at 6 km then started a spiral descent (between 09:35 and 09:59 UTC, and reached the marine boundary layer where it continued with a level flight at 300 m.

ACPD
11, 13525–13574, 2011

The sky was then cloud-free around the plane, which simplifies the radiative transfer calculations and reduces considerably the uncertainties in the results. During the second sounding, the plane, flying at 5 km altitude, started its descent at 09:44 UTC and reached its lowest altitude (250 m) at 10h04. Some clouds were present close to the sea surface.

3 Spectral analysis and profiling method

The data analysis consists mainly of three steps: (1) quantification of O_4 and NO_2 molecular absorptions in the spectra, (2) retrieval of the vertical distributions of aerosol extinction and NO_2 concentration from these measured absorptions and (3) error budget.

The first step is achieved with the DOAS technique (Platt and Stutz, 2008) which disentangles specific absorptions from other contributions in the spectra. These absorptions do not depend only on aerosol extinction and NO_2 concentration but also on other geophysical parameters and on the measurement geometries. The second step involves a modeling of the atmospheric radiative transfer to study the sensitivity of the measurements to aerosol extinction and NO_2 concentration and a regularization method to solve the inverse problem of retrieving those quantities. We use the maximum a posteriori solution as described in Rodgers (2000), which also provides a rigorous error analysis.

3.1 DOAS analysis

Molecular absorptions such as those of O_4 and NO_2 are commonly retrieved in uv-visible atmospheric spectra using the DOAS technique. This method relies on the fact that their absorption cross-sections vary much more rapidly with wavelength than the scattering effects (Rayleigh and Mie). In practice, a measured spectrum ($I(\lambda)$) is divided by a reference one ($I_{ref}(\lambda)$) to remove solar Fraunhofer structures and reduce

ACPD
11, 13525–13574, 2011

instrumental effects. The slow variations in this ratio are filtered out with a low-order polynomial ($P(\lambda)$) and the remaining absorption structures are fitted in a least-square sense with high-pass filtered laboratory cross-sections ($\sigma'_i(\lambda)$). DOAS enables thus to apply the Beer-Lambert law in the atmosphere, in a form that can be written as:

$$\ln \frac{I(\lambda)}{I_{\text{ref}}(\lambda)} = -\sum_i \sigma'_i(\lambda) \cdot \text{DSCD}_i + P(\lambda) \quad (1)$$

In the above equation the index i represents one particular absorber. DOAS analysis results are, for each considered absorber, differential slant column density (DSCD), i.e. the differences between the concentration integrated along the optical path of the measurement and the corresponding quantity in the reference spectrum.

Table 1 lists the DOAS analysis settings used for the retrievals of O_4 and NO_2 DSCDs. These settings were implemented in the QDOAS software, developed by our group (http://uv-vis.aeronomie.be/software/QDOAS). The molecular cross-sections references are in the table except for O_4 for which we use the Hermans version (http://www.aeronomie.be/spectrolab/o2.htm). The Ring effect (Grainger and Ring, 1962) originates from rotational Raman scattering by O_2 and N_2 and produces a filling-in of solar Fraunhofer lines in scattered light. We fit a Ring pseudo-absorption as described in Chance and Spurr (1997) to take it into account.

Figure 3 presents a typical NO_2 DOAS result. The spectrum was recorded when the aircraft was flying inside the marine boundary layer during the flight as0831. It shows the NO_2 fit (panel a), the water vapor optical density (panel b) which contributes significantly to the signal at the end of the analysis spectral window, the Ring effect (panel c) and the fit residuals (panel d). Note that the pixels between 435.4 and 436.5 nm are damaged and therefore not considered in the DOAS fit.

3.2 Radiative transfer modeling

The DSCDs obtained with the DOAS analysis depend on the light path, which is different for every single observation due, e.g. to the telescope scanning. Moreover, for

ACPD
11, 13525–13574, 2011

scattered sky-light as in our experiment, multiple unknown photon paths contribute to the signal simultaneously. Modeling the radiative transfer in the atmosphere enables us to define an effective light path necessary to interpret the measurements.

The radiative transfer model we use here is UVspec/DISORT (Mayer and Kylling, 2005). It is based on the discrete ordinate method and deals with multiple scattering in a pseudo-spherical approximation. Radiances at a given wavelength and absolute slant column densities (SCD) for molecules of interest can be calculated, for a geometry and a predefined atmospheric state. Considering our DOAS fitting windows, the calculations were done at 360 and 440 nm respectively for O_4 and NO_2. The quantity retrieved with DOAS being a differential SCD, the reference SCD (SCD_{ref}), i.e. the integrated concentration along the optical path in the reference spectrum, must be determined (cf Sect. 4.1).

Some of the atmospheric state parameters, usually sources of uncertainties in the retrieval of a particular geophysical quantity, were measured in situ onboard the plane, like the temperature, pressure and ozone concentration. We use these measured profiles in our model, completed higher up in the troposphere and in the stratosphere with values extracted from the TOMSV8 climatology (McPeters et al., 2007). The latter uses as input the ozone total column, estimated at 390 Dobson units in our case from the AURA AVDC values at Ny-Ålesund and Tromsø (http://avdc.gsfc.nasa.gov/). The NO_2 profile is built from the TM4 model (Boersma et al., 2007), the stratospheric part being scaled to reproduce the stratospheric vertical column measured by the OMI instrument. The albedo of open-water can be calculated accurately assuming a Fresnel reflection (Brandt et al., 2005) which leads to an albedo value of 0.1 for 65° solar zenith angle. This value depends on the refractive index of water which is almost constant between 350 and 450 nm so the same albedo value was used for the two wavelengths. The aerosol optical properties (extinction, absorption and asymmetry parameter) are estimated using the OPAC software package (see next section).

The observation geometry is not constant during a measurement due to the circular flight pattern and the 30 s accumulation time. In particular the relative azimuth angle

ACPD
11, 13525–13574, 2011

varies by up to 30°. To overcome this problem we calculate each SCD as a weighted mean of 9 intermediary SCDs, the weights being the different radiances calculated in the respective intermediate SCD geometries, defined by the corresponding orientations of the aircraft and solar positions.

Once the atmospheric state and the geometry are defined, the sensitivity of the measurement to a parameter $\boldsymbol{x}$ can be expressed as the derivative $\frac{\partial \mathrm{SCD}}{\boldsymbol{x}}$. For a vertical distribution $\boldsymbol{x} = \boldsymbol{x}_{i=1\ldots n}$, e.g. of NO_2, the weighting function is the sensitivity of a measurement to the values of the distribution in the layers $\frac{\partial \mathrm{SCD}}{\partial \boldsymbol{x}_i}$. Weighting functions are compulsory to retrieve vertical distributions. We calculate them by perturbations on the predefined profiles of extinction and NO_2. In addition to the linear weighting functions ($\frac{\partial \mathrm{SCD}_{O_4}}{\partial \mathrm{ext}_i}$, $\frac{\partial \mathrm{SCD}_{NO_2}}{\partial [NO_2]_i}$), we also calculate logarithmic weighting functions ($\frac{\partial \mathrm{SCD}_{O_4}}{\partial \ln \mathrm{ext}_i}$, $\frac{\partial \mathrm{SCD}_{NO_2}}{\partial \ln [NO_2]_i}$). This enables us to constrain the retrievals to positive values (see next section).

Figure 4 shows typical NO_2 weighting functions for the sounding of the flight as0831 (8 April 2008). While the shapes are different for the linear and logarithmic approaches, both indicate a sensitivity across the whole sounding altitude range. For viewing angles close to the horizon (90°), the sensitivity is maximum at the altitude of observations due to the enhanced light path in this layer. The maximum absolute values vary in opposite way with the observation altitude: they tend to increase for the linear case whereas they decrease for the logarithmic one. In the first case, it is due to the reduced scattering at high altitude: as aerosol and Rayleigh scattering decrease the light path increases. In the second case, this effect, still present, is dominated by the decrease of sensitivity to the logarithm for smaller concentrations, as most of the NO_2 in the predefined profile is assumed to be in the boundary layer. Indeed, for small $[NO_2]$ values, $\partial \ln [NO_2]$ gets large and reduces thus the derivative $\frac{\partial \mathrm{SCD}_{NO_2}}{\partial \ln [NO_2]_i}$).

Dividing the linear weighting functions by the layers thickness defines the box air mass factors (box AMF, Wagner et al., 2007). The box AMF scale is also displayed on Fig. 4 and can be compared with the same quantity calculated for nadir looking satellites (e.g. by Zhou et al., 2009, Fig. 1) and ground-based MAX-DOAS instruments

ACPD
11, 13525–13574, 2011

(e.g. by Wittrock et al., 2004, Fig. 4). In the OMI case, Zhou et al., 2009 indicates a box air mass ranging from unity toward the ground to two in the high troposphere. The MAX-DOAS is most sensitive close to the ground when its telescope points just above the horizon. The box AMF, around 20, is then comparable to airborne limb measurements. But this sensitivity decreases rapidly with altitude contrary to our airborne set-up, which indicates that this approach is particularly well suited for the study of the free troposphere.

3.3 Retrieval of the geophysical quantities with a maximum a posteriori evaluation

The weighting functions express the sensitivity of a measurement to a vertical distribution $\boldsymbol{x}$, or more accurately their respective variations. For a set of measurements $\boldsymbol{y}$ $\boldsymbol{y}_{j=1\ldots m}$, defining the weighting functions matrix $\mathbf{K}$ as $\frac{\partial \mathrm{SCD}_j}{\partial \boldsymbol{x}_i}$ enables to write, if $\boldsymbol{x}$ is close to the linearization point $\boldsymbol{x}_0$:

$$\boldsymbol{y} - \boldsymbol{y}_0 = \mathbf{K}\,(\boldsymbol{x} - \boldsymbol{x}_0) + \epsilon \tag{2}$$

where $\boldsymbol{y}_0$ represents a measurement series at the linearization point $\boldsymbol{x}_0$, which can be calculated with the radiative transfer model.

Due to the error ϵ, which represents instrument noise and model uncertainties, the solution $\hat{\boldsymbol{x}}$ is a statistical estimate of the true state. The problem is generally ill-posed and some regularization is required to retrieve $\hat{\boldsymbol{x}}$. We use the maximum a posteriori solution as presented in Rodgers (2000), often referred as "optimal estimation". It requires a priori knowledge of the quantity to retrieve and assumes Gaussian statistics for this a priori and the error. The solution with maximum probability after the measurements (a posteriori), due to the non-linearity of the problem, must be reached by iterations, e.g with the Gauss-Newton algorithm:

$$\boldsymbol{x}_{i+1} = \boldsymbol{x}_i + (\mathbf{S}_\mathrm{a}^{-1} + \mathbf{K}_i^T \mathbf{S}_\epsilon^{-1} \mathbf{K}_i)^{-1} [\mathbf{K}_i^T \mathbf{S}_\epsilon^{-1} (\boldsymbol{y} - \mathbf{F}\,(\boldsymbol{x}_i)) - \mathbf{S}_\mathrm{a}^{-1}\,(\boldsymbol{x}_i - \boldsymbol{x}_\mathrm{a})] \tag{3}$$

ACPD
11, 13525–13574, 2011

where $\mathbf{S}_a$ and $\mathbf{S}_\epsilon$ are respectively the a priori and error covariance matrix, and $\mathbf{K}_i$ the weighting functions matrix calculated with the vertical distribution $\boldsymbol{x}_i$.

After convergence, the solution is a weighted mean of the a priori knowledge and the information coming from the measurement. The averaging kernels matrix $\mathbf{A}$ measures this weight, its trace being the number of independent information retrieved, namely the degree of freedom for the signal (dofs):

$$\mathbf{A} = (\mathbf{K}_i{}^T \mathbf{S}_\epsilon^{-1} \mathbf{K}_i + \mathbf{S}_a^{-1})^{-1} \mathbf{K}_i^T \mathbf{S}_\epsilon^{-1} \mathbf{K}_i \quad (4)$$

The averaging kernels matrix contains also information about the vertical resolution of the retrieval: for a given level, it is estimated from the full width at half maximum (FWHM) of the main peak of the corresponding averaging kernel.

To save computing time, we do not recalculate the weighting function matrices $\mathbf{K}_i$ after each iteration, as suggested in Rodgers (2000). This approximation seems reasonable since the real state is close to the linearization point. Moreover $\mathbf{S}_a$ is used here as a tuning parameter, to optimize the dofs while preventing non-physical values and oscillations in the retrieved profiles.

For both extinction and NO_2 retrievals, vertical distributions corresponding to a priori, linearization point and starting point of the Gauss-Newton iterations are the same. For the first sounding (8 April 2008), the chosen altitude grid extends from 0 up to 8 km in steps of 0.5 km each, except for the lowest step which is 1 km thick. For the second sounding (9 April 2008), clouds prevent us to model the radiative transfer in the lower part of the atmosphere and, therefore, the grid starts at 3 km and the layers are 1 km thick up to 8 km.

The a priori on aerosol extinction profiles are constructed with the software package OPAC (Optical properties of Aerosol and Clouds, Hess et al., 1998). OPAC assumes ten types of spherical particles that can be mixed to reproduce typical aerosol conditions and provides their optical properties in the solar and terrestrial spectral range as a function of relative humidity. Conveniently, one of these predefined mixtures corresponds to the Arctic spring, and the relative humidity was measured in situ during the

ACPD
11, 13525–13574, 2011

flight. Figure 5 shows an a priori extinction profile built from the OPAC output at 350 nm together with measured relative humidity.

For the NO_2 retrieval, the extinction profile at 360 nm retrieved from O_4 DSCDs is corrected to take into account the scattering reduction in the visible with OPAC Angstrom coefficients. The a priori NO_2 vertical distribution is extracted from the corresponding TM4 vertical distributions available with the DOMINO (Dutch OMI NO_2) product (http://www.temis.nl/airpollution/no2col/no2regioomi_v2.php).

The assumption of Gaussian statistics, needed to establish Eq. (3) is realistic for the instrument noise but less obvious for the quantity to retrieve. For positive geophysical quantities with large variability around a small mean, a significant part of the probability density lies in the negative range which is unphysical. Retrieving the logarithm of the quantity, i.e. assuming a lognormal probability distribution, can overcome the problem. It implies to calculate logarithmic weighting functions, as described in the previous section. This has been done already e.g. for water vapor (Schneider et al., 2006), and CO (Deeter et al., 2007). For these two species, the authors further indicate that in situ measured statistics are closer to lognormal distributions. We compare the results of both methods in Sect. 4.

3.4 Error analysis

The uncertainties in the retrieval originate from three sources: the instrument noise, the uncertainties in the model parameters which are not retrieved (e.g. albedo) and the finite vertical resolution of the retrieval. The error from the model itself is neglected, which seems reasonable from previous intercomparison exercises (Hendrick et al., 2006).

The two first sources limit the accuracy in relating a profile $\boldsymbol{x}$ to a set of measurements $\boldsymbol{y}$ and correspond to the measurement error ϵ in Eq. (2). The associated error covariance matrix is calculated from the noise covariance ($\mathbf{S}_N$) and the model

ACPD
11, 13525–13574, 2011

parameters covariance ($\mathbf{S}_b$) according to:

$$\mathbf{S}_\epsilon = \mathbf{S}_N + \mathbf{K}_b \mathbf{S}_b \mathbf{K}_b^T \quad (5)$$

where $\mathbf{K}_b$ is the matrix of sensitivities to the model parameters, constructed by perturbations on these parameters.

The noise covariance $\mathbf{S}_N$ is built with the square of the error in the slant columns, which is an output of the DOAS analysis depending on the fit residuals, the off-diagonal elements are neglected.

Retrieving O_4 profiles in a similar experiment, Prados-Roman et al. (2010) identified the albedo and the asymmetry parameter as major sources of model parameter errors. We introduce uncertainties on these parameters with respective standard deviations of 0.02 and 0.01. To take into account the O_4 cross-section uncertainties (see Sect. 4.1), another error source was introduced corresponding to 2 % of the measured DSCD. For the NO_2 retrieval, we consider uncertainties with respect to the albedo ($\sigma = 0.02$) and on the aerosol extinction, with standard deviations estimated from our extinction retrieval.

The measurement error, with its covariance $\mathbf{S}_\epsilon$ is propagated in the retrieval with the gain matrix $\mathbf{G}$ defined as $(\mathbf{K}^T \mathbf{S}_\epsilon^{-1} \mathbf{K} + \mathbf{S}_a^{-1})^{-1} \mathbf{K}^T \mathbf{S}_\epsilon^{-1}$, representing the relationship between the retrieval and the signal. The corresponding retrieval error covariance is thus expressed as:

$$\mathbf{S}_R = \mathbf{G} \mathbf{S}_\epsilon \mathbf{G}^T \quad (6)$$

The retrieval is a smoothed version of the true profile. This finite vertical resolution is the third error source and is calculated as:

$$\mathbf{S}_S = (\mathbf{A} - \mathbf{I})\, \mathbf{S}_{var}\, (\mathbf{A} - \mathbf{I}) \quad (7)$$

where $\mathbf{S}_{var}$ is the natural variability covariance and $\mathbf{I}$ the identity matrix. Natural variability is often difficult to quantify. For the extinction, we estimate it from AOD measurements between 1995 and 1999 at Ny-Ålesund (Herber et al., 2002). This study

ACPD
11, 13525–13574, 2011

presents statistics for measurements at 532 nm for different seasons and conditions. The background (no Arctic Haze) spring value is 0.067 ± 0.017. Considering this, the variability covariance matrix is built assuming standard deviations of 0.005 in all the layers with relative humidity larger than 50 %, no correlations is considered between the layers. For NO_2, natural variability in the free troposphere is derived from the TOPSE aircraft campaign. Stroud et al. (2003) give statistics for the NO_x measurement during the campaign: a mean and standard deviation of 17 ± 13 pptv. Interestingly the median is also calculated and its value, 15 pptv, is smaller than the mean, which is typical of a lognormal distribution. We use the standard deviation of these NO_x measurements. Again, no off-diagonal elements are added to the variability covariance matrix. Figure 6 displays the different error sources and their propagation in the aerosol extinction retrieval on 8 April 2008. The error profiles for each parameter represent the square root of the diagonal elements of its covariance matrix. It is noteworthy that the main error source on the measurements, the albedo, is insignificant after the retrieval. The total uncertainty appears dominated by the smoothing error.

4 Results for the soundings on 8 and 9 April 2008

In this section, we present the O_4 and NO_2 DSCD measured during the flights as0831 (8 April 2008) and as0833 (9 April 2008) and the corresponding retrieved aerosol extinction and NO_2 concentration profiles, for which we compare the linear and logarithmic approach. Between these two steps, we make sure the measurements are qualitatively reproduced by the radiative transfer model and use the latter to infer in particular the residual columns in the reference spectrum and a detection limit for NO_2.

4.1 Residual slant columns and O_4 cross-section scaling factor

As described in Sect. 3.1, our DSCD measurements are relative to the slant column in a reference spectrum. Determination of this reference column is thus necessary

ACPD
11, 13525–13574, 2011

for any further quantitative discussion on geophysical quantities. O_4 and NO_2 DSCDs presented in the following are relative to their respective columns in the same spectrum, selected at the top of the as0831 sounding, near 6 km altitude. For both species the reference slant column is estimated comparing high altitude DSCD measurements with calculated SCDs. We make the assumption that the geophysical quantities to be retrieved do not affect significantly the slant column calculation at high altitude, which we believe is a reasonable hypothesis based on sensitivity tests using the radiative transfer model.

There remain some uncertainties regarding the absolute value of the O_4 absorption cross-section and measured DSCDs are commonly corrected with ad hoc scaling factors to retrieve extinction. During an intercomparison exercise involving four MAX-DOAS instruments, Zieger et al. (2010) reported scaling factors from 0.75 to 0.83. Spectra obtained at high altitudes give an opportunity to estimate accurately such a scaling factor. Indeed, the O_4 vertical distribution depends only on the air density, which can be calculated from pressure and temperature measured onboard the plane. Moreover, aerosol scattering, the major uncertainty source in O_4 SCD calculations, can be neglected above 6 km and this is confirmed by comparing measurements and simulations.

To quantify the O_4 residual slant column in the reference spectrum (SCD_{ref}) and the cross-section factor (α), we apply a linear regression between measured DSCD and calculated SCD in the same geometries:

$$SCD = \alpha \cdot DSCD + SCD_{ref} \quad (8)$$

Figure 7 shows the fit results for two O_4 DSCD series measured when the aircraft was flying above 5.5 km. The modeled atmosphere neglects aerosol scattering but uses the in situ measurements (pressure, temperature, ozone) during the sounding. The O_4 vertical distribution is calculated from the observed pressure and temperature. This leads to a scaling factor α of 0.89. DSCD measurements used to retrieve the aerosol extinction coefficient were therefore scaled by this value, which is higher

ACPD
11, 13525–13574, 2011

than the values reported by Zieger et al., 2010, but closer to the direct-sun measurements of Spinei (see http://www.knmi.nl/omi/documents/presentations/2010/ostm15/OSTM15_AIS_Spinei_O2-O2_Cross_Sections.pdf).

For NO_2 measurements, we use the same high-altitude series to estimate a reference SCD, without fitting a correction factor on the cross-section. This leads to a NO_2 reference column of 7.81×10^{15} molec cm^{-2}. Aerosol optical effects are also neglected and the NO_2 profile used is taken from the TM4 model (see Sect. 3.2).

4.2 Measured versus simulated slant columns

In Fig. 8, O_4 and NO_2 measured DSCDs are compared with simulations for the spectra recorded between 09:16 and 10:01 UTC during the as0831 flight. The upper panel shows the aircraft altitude and the telescope line-of-sight angle. During the considered period, the aircraft was flying at high altitude (6 km) before descending to the marine boundary layer and continuing with a level flight at 300 m. The two lowest panels display the measured and simulated O_4 and NO_2 DSCD series. The telescope kept scanning during the whole period, which explains the variations in the DSCDs. These oscillations are qualitatively reproduced by the simulations, which indicates the radiative transfer in the model atmosphere approximates correctly the measurements. The O_4 slant column series are closer to the simulations than the NO_2, especially at high altitude, due to the weak aerosol extinction there and the known vertical distribution of O_4

The oscillations are anticorrelated for the two species during the high altitude part. This is due to the fact that the NO_2 signal is then dominated by the stratospheric contribution (see Sect. 4.3), and thus maximum when the telescope points upward, while the O_4 concentration is largest at the ground, and so DSCD is highest when the telescope looks downward. The altitude dependence is also different for the two species. The O_4 DSCD, beside the oscillations, systematically increases during the descent, which is expected from the increase of air density. In the boundary layer where the aerosol extinction limits the optical path, the DSCD decreases again. In contrast, the NO_2 is

ACPD
11, 13525–13574, 2011

stable during the descent but increases only in the boundary layer, indicating a very low NO_2 concentration in the free troposphere and higher values close to the sea surface.

Deviations between measured and simulated DSCDs indicate differences between the true state of the atmosphere and the radiative transfer parameters used. This is visible at the end of the two DSCD series, corresponding to the boundary layer. In this region, aerosol extinction is no more negligible and the NO_2 concentration is higher than the one in the model atmosphere.

4.3 NO_2: Influence of the stratosphere and detection limit

For NO_2, the SCD simulations reveal a substantial influence of stratospheric NO_2 overhead although our measurements were performed in the troposphere. This effect can be clearly identified in Fig. 9, which compares measured NO_2 DSCDs during the sounding and simulations with and without taking into account the stratospheric part. The effect is particularly visible at higher altitudes where discrepancies between the measurements and simulations without the stratospheric part are larger than discrepancies when taking into account the stratosphere. Since the NO_2 concentration is low in the free troposphere, the signal originates mostly from the stratosphere and the boundary layer, where a NO_2 layer is detected (see previous section). The stratospheric influence is largest when the telescope points upward, towards the stratosphere, whereas the opposite is valid for the boundary layer.

To constrain the stratospheric NO_2 content in our simulations, we have used measurements of stratospheric NO_2 columns obtained from the OMI satellite instrument, which was flying above the sounding area, precisely at 9h42m on the orbit 19850. Assimilated vertical stratospheric column (2.91×10^{15} molec cm^{-2}) from the DOMINO data product (see Sect. 3.3) have been used to scale to the TM4 vertical distribution in the stratosphere.

We estimate the minimum detectable DSCD as corresponding to an optical density of two times the DOAS fit residual root mean square deviation (RMSD). Converting

ACPD
11, 13525–13574, 2011

this minimum DSCD to a vertical column density requires the knowledge of the enhancement factor between the VCD and the DSCD, namely the air mass factor (AMF), which can be derived from simulations. The detection limit is thus $\frac{2\mathrm{RMSD}}{\mathrm{AMF}\sigma}$ where σ is the NO_2 cross-section value. With a RMSD of around 2.1×10^{-4} (Fig. 3) and an AMF in the boundary layer of around 10, the minimum detectable vertical column is 7.3×10^{13} molec cm^{-2}. Assuming a homogeneous 1 km thick layer, this corresponds to a concentration of 6.6×10^{8} molec cm^{-3} and a volume mixing ratio of 27 pptv. Taking the NO/NO_2 ratio of 0.5 given by Ridley et al. (2000) in similar conditions, this leads to a total NO_x mixing ratio of 40 pptv. These detection limits are below the 50 pptv achieved with commercial airborne chemiluminescent analyzers (Ancellet et al., 2009).

4.4 Retrievals of aerosol extinction coefficient and NO_2 concentration

Preliminary retrievals demonstrated the difficulty to reproduce quantitatively the measurements corresponding to the telescope pointing slantwise downward when the aircraft is at low altitude. A similar problem has been mentioned for DOAS ground-based measurements in the same region (Wittrock et al., 2004). Increasing the albedo improves the situation for these points but deteriorates it for the others. Wittrock et al. suggested that the presence of thin clouds might explain the problem. Such clouds were not noticed during this part of the flight so the problem could arise from another cause, e.g. a small BRDF effect on the albedo. The measurements below the horizon were not considered for the retrievals.

Figure 10 shows the retrievals of the vertical distribution of aerosol extinction coefficient for the sounding at 71° N, 22° E on 8 April 2008. The panels a and b correspond to the linear retrieval, i.e., assuming Gaussian statistics on the a priori, the panels c and d to the logarithmic retrieval and the lognormal a priori (see Sect. 3.3). Averaging kernels (panels a and c) are different for the two methods. They do not represent the same quantity in linear and logarithmic scale but indicate that the logarithmic retrieval is more strongly constrained by the measurements than the linear one, the

ACPD
11, 13525–13574, 2011

dofs being respectively 4.6 and 2.06. For the linear case, the averaging kernels get very close to zero above 3 km altitude, where the a priori extinction is 0.001. The retrieved profiles are similar below 3 km altitude, with an extinction in the boundary layer of $0.04 \pm 0.005\,\mathrm{km}^{-1}$. Above 3km altitude the linear retrieval, due to the averaging kernels, remains close to the a priori profile, whereas the logarithmic retrieval exhibits a layer with enhanced extinction ($0.01 \pm 0.003\,\mathrm{km}^{-1}$) around 4 km altitude.

For the linear case, the loss of sensitivity to the measurements above 3km is explained by the low a priori extinction in these layers. As mentioned in Sect. 3.3, the a priori covariance matrix ($\mathbf{S}_a$) we use is diagonal, each element being the variance of the aerosol extinction in the considered layer. Tuning these variances to optimize the retrieval is a trade-off: large variances lead to small constrains of the a priori compared to the measurements and thus higher dofs, but it implies to consider negative values of the probability density function as non-negectable if the standard deviation, i.e. the square root of the variance, gets close to the mean, i.e. the apriori extinction in $\boldsymbol{x}_a$. This is first the case for small a priori extinction values, i.e. the ones above 3 km altitude. Negative aerosol extinction values are non-physical and not supported by our model. It was thus necessary when building the $\mathbf{S}_a$ matrix to set variances small enough to avoid negative values, especially above 3 km altitude, reducing the sensitivity in these layers.

We show in the same figure an extinction profile calculated from the measured aerosol size distribution (see Sect. 2.2) using a Mie scattering model (Matzler, 2002; Bond et al., 2006). We assume in the calculation a constant complex refractive index of $1.5 + 0.01i$, a value taken from Tomasi et al. (2007). One of the aerosol samplers, the PCASP which measures the aerosol size distribution between 0.1 and 3 microns, could not be completely calibrated during the campaign. The missing calibration mainly affects aerosol extinction calculated for the marine boundary layer, where large sea-salt aerosols may be present. Nevertheless, the Mie calculation provides information about the shape of the true profile. The enhanced extinction layer at 4 km altitude in the Mie calculated profile is obtained only with the logarithmic retrieval. The same holds true for

ACPD
11, 13525–13574, 2011

the second flight, indicating that a lognormal assumption on the density of probability of extinction can be useful for its retrieval.

The drawbacks of the retrieval scheme are first a slower convergence; it takes generally two iterations for the linear retrieval and five for the logarithmic one, which may come from a smaller degree of linearity in the logarithmic statement of Eq. (2) as mentioned by Schneider et al. (2006) for water vapor retrievals. A second limitation lies in a probable underestimation of the errors when the retrieved value is low, as above 5 km in Fig. 10. This is due, as the sensitivity reduction with extinction described in Sect. 3.2, to the logarithmic behavior toward small values. Indeed, in Figs. 10, 11 and 12, error bars correspond to the square root of the diagonal elements of the total error covariance matrix. Converting a logarithmic error covariance ($\mathbf{S}_{\ln x}$) to a linear one ($\mathbf{S}_x$) often implies a Taylor expansion leading to the simple expression $\mathbf{S}_x = \boldsymbol{x}\mathbf{S}_{\ln x}\boldsymbol{x}$, as detailed in (Dubovik et al., 1995). It is clear from this expression that for small values the associated covariance is small. In our case, we do not apply the Taylor expansion and use the exponential of the logarithmic error, but the problem is the same. These problems and a more detailed analysis of what the lognormal assumption for the extinction retrieval from DOAS measurements deserve further attention, but this is outside the scope of this paper.

Figure 11 shows the retrievals of the vertical distribution of the NO_2 concentration during the same sounding on 8 April 2008. In this case, the linear and logarithmic approaches yield similar results. The averaging kernels indicate a rather constant sensitivity for the whole sounding with typical dofs of 5.3 and 5.7 for the linear/logarithmic case. Three zones are distinguishable, the boundary layer with a concentration of $1.9 \pm 0.3 \times 10^9$ molec cm^{-3}, the lower free troposphere with around $3 \pm 1 \times 10^8$ molec cm^{-3} between 1 and 4 km altitude and the higher troposphere with negligible concentrations. In the boundary layer the corresponding NO_2 volume mixing ratio is 66 ± 19 pptv, well above the detection limit of 40 pptv calculated in the previous section. No in situ measurements are available to be compared with but integrating the profile leads to a tropospheric column of 1.99×10^{14} molec cm^{-2}. The OMI tropospheric

ACPD
11, 13525–13574, 2011

column extracted from the DOMINO product at the sounding time above the area is $1.705 \pm 6.146 \times 10^{14}$ molec cm^{-2}. This value appears close to our measurement but it lies inside the error bars which indicates that such low concentrations are not detected by OMI.

Figure 12 presents the extinction and NO_2 retrievals for the sounding at 70° N, 17.8° E on 9 April 2008. The radiative transfer was complicated by clouds close to the surface, thus our retrievals start at 3 km altitude. We use the logarithmic case for the extinction retrieval. The dofs value is low (0.27) but nevertheless the retrieved profile is distinctly different from the a priori and exhibits an extinction maximum, 0.025 ± 0.005 km^{-1} at 4 km altitude, which is also visible in the extinction calculated from the size distribution. A maximum in the NO_2 concentration of $1.95 \pm 0.2 \times 10^9$ molec cm^{-3} is also observed at the same altitude. For this NO_2 retrieval, the dofs value is 1.44.

5 Interpretation of the retrieved profiles

Figure 13 shows in situ measurements of ozone and CO during the two studied soundings and total attenuated backscatter ratio (R) measured with the lidar at 532 and 1064 nm. This quantity, described in de Villiers et al. (2010, Appendix. A), tends to unity when aerosol loading decreases. For the second sounding, the lidar profile was measured at 11:40 UTC above 69.6° N, 19° E i.e. two hours and 60 km off the sounding because the clouds mentioned in the previous section disturbed the measurements at the sounding time. CO can serve as a pollution tracer due to its long life time (around 20 days in the free troposphere; Forster et al., 2001) and has both anthropogenic and natural sources, many of them correlated to the sources of NO_2 and aerosols. The first sounding (8 April 2008) exhibits anticorrelated variations of ozone and CO volume mixing ratio (vmr) around the altitude where we measure an extinction enhancement in the free troposphere. A layer with 15 ppbv of CO above the 3 km altitude level (150 ppbv) around 3.7 km altitude corresponds to a reduction of ozone of the same order of magnitude. At 4.2 km altitude, the situation is opposite: a layer with higher ozone vmr

ACPD
11, 13525–13574, 2011

(40 ppbv above background) corresponds to a 25 ppbv reduction of CO vmr. Above 4.5 km altitude, weaker structures are still visible in the ozone profile. The lidar profile clearly shows the boundary layer, with R values for 1064 nm of 2.8 at 0.8 km altitude, and other layers in the free troposphere, in particular at 4.3 km altitude, where R is around 1.8. During the second sounding (9 April 2008), ozone is increasing smoothly from 50 to 60 ppbv with height, but CO presents two layers with enhanced vmr, around 2.7 km (+35 ppbv) and from 3.5 km to 5 km (+50 ppbv). These layers are correlated with enhancement of the R values (respectively 2.3 and 1.8)

Anticorrelations between higher ozone concentration and CO have been observed in previous aircraft measurements (Zahn et al., 2000; Stohl et al., 2007) and explained by a stratospheric origin of the observed air or mixing with stratospheric air. The extinction layer around 4 km detected by our measurement on the first sounding is unlikely to come from the stratosphere since the background extinction observed there is one order of magnitude smaller (Vanhellemont et al., 2010) and no major volcanic eruptions were reported before the period of the campaign. From the lidar profile, it is not obvious either if the structure at 3.7 km altitude with higher CO corresponds to our extinction maximum. Indeed, this one is probably at the altitude of the R maximum, 4.3 km, even if it appears lower with the low vertical resolution of our retrieval achieved at this altitude, seen from the width of the averaging kernels in Fig. 10. On the second flight, the situation is clearer: a layer with high CO vmr and backscatter ratio occurs where our retrieved profiles of extinction and NO_2 are maximum.

Figure 14 presents for both flights backward air mass trajectories calculated using the HYSPLIT (HYbrid Single-Particle Lagrangian Integrated Trajectory) model (Draxler and Hess, 1998) with the GDAS meteorological data serving as input. To understand the vertical variability around 4 km altitude in the two cases, the calculations start at 3.6, 4 and 4.4 km altitude for both soundings and consider a period of 10 days. The first sounding shows an interesting mixing of high and low altitude air masses: the air at 4 km appears to come from the boundary layer close to Iceland and is sandwiched between two air masses originating from higher up in the atmosphere. At 4.4 km height,

ACPD
11, 13525–13574, 2011

the air originates from above the North pole and stayed mainly above 7 km altitude during the last 10 days, which agrees with the high measured ozone mixing ratios. The measurements of the first sounding can thus be explained by a mixing of stratospheric and boundary layer air masses. The second sounding is again easier to interpret: the air mass at 4 km altitude originate from the central European boundary layer, where it has been lifted two days before the measurements. This back-trajectory explains the more polluted air mass of the second flight in the free troposphere, with higher CO and aerosol extinction, compared to the corresponding air mass in the first sounding.

The presence of the short-lived NO_x in the Arctic is usually explained from local sources, such as peroxyacetic nitric anhydride (PAN) decomposition (Stroud et al., 2003), ships (Wittrock et al., 2004) or snow photochemistry (Honrath et al., 1999). The back-trajectories of Fig. 14 tend to eliminate the last two options for the free tropospheric NO_2 observed during the second flight. The air does not come from a close marine or snow-covered boundary layer. Considering PAN decomposition, which occurs mostly in summer (Beine and Krognes, 2000), the temperature at the altitude of the detected layer, 255 K is too low for it to be significant (Stroud et al., 2003). These considerations and the correlations between the CO, aerosol extinction and NO_2 layer suggest that this NO_2 was directly transported from pollution source regions in Europe. The lifetime of NO_2 depends on the meteorological conditions and the oxidizing capacity of the atmosphere but can be approximated as decreasing exponentially with the surrounding air mass temperature. According to the study of Dils (2008) and with an in situ temperature of 255 K, this lifetime is 2.14 days. This result is close to the lifetime of NO_x presented in Stroud et al. (2003), which is above 2.5 days. The back-trajectory of the second flight indicate that the air mass was in a polluted boundary layer 2 days before the measurement, which supports the idea of transported NO_2.

We also ran the Lagrangian Particle Dispersion Model (LPDM) FLEXPART version 8 (Stohl et al., 2005) 20 days backward from short segments along all campaign flights (see http://transport.nilu.no/flexpart-projects?cmp=POLARCAT_FRANCE). The output of these calculations are emission sensitivities (Stohl et al., 2003), which can be used

ACPD
11, 13525–13574, 2011

to interpret transport processes and to identify potential pollution source regions. When ignoring removal processes and multiplying the emission sensitivities with emission flux densities of CO and NO_x, we obtain maps of source contributions, identifying the areas where pollution sources contributed to the sampled air mass. The emission data was taken from the EDGAR v32 database (Olivier et al., 2005) globally but EMEP emissions were used for Europe. Browsing the source contributions along the soundings, local maxima are found for the CO source contributions close to the altitude where the in situ sounding vmr are the highest. For the second flight, the NO_2 source contribution is maximal at 4 km altitude. According to Fig. 15, NO_2 is released in the same regions as CO, namely over Europe, especially over Poland. The total simulated CO mixing ratio of 57 ppbv accumulated for 20 days prior to the sounding is close to the measured CO enhancement over the background. During the first flight, the simulated CO tracer enhancement is less than 9 ppbv, in agreement with the small measured CO enhancements. In this case, CO sources located in Northwestern Europe are responsible for the detected CO enhancement. Notice that the simulated total NO_x tracer measurements are much higher than the measured NO_2 because NO_x has a much shorter lifetime than the 20 days over which emissions are accumulated in the model. In reality, only a fraction of the NO_x emitted over the last 20 days is transported to the measurement location and only a fraction of it is present as NO_2.

Considering the boundary layer NO_2 observed during the first flight, footprint emission sensitivities shown in Fig. 16 indicate that the surface areas influencing the air mass are Northern Lapland, parts of the Kola peninsula and Barents Sea. While FLEXPART does not indicate a large CO or NO_2 source contribution from these areas, transport times from the Kola Peninsula were less than 1 day and even the small (1 ppbv) simulated NO_2 tracer mixing ratio (originating mostly from the Kola Peninsula) is much higher than the measured NO_2 mixing ratio. Furthermore, emissions on the Kola Peninsula are notably uncertain, with known errors in the emission inventories used (Prank et al., 2010). In particular, emissions in Nikel in the western Kola Peninsula, which the observed air mass traversed, are too low and appear erroneously

ACPD
11, 13525–13574, 2011

attributed to Murmansk in the inventories (Prank et al., 2010). Emissions from the smelters there are sulfur-rich, so that it is likely that the observed aerosols are mainly sulfate. The smelter emissions are relatively poor in CO, so the small measured CO enhancements are not contradictory to this source.

6 Conclusions

We have retrieved vertical distributions of aerosol extinction coefficient and NO_2 concentration using a novel airborne DOAS instrument flown on board the ATR-42 during the POLARCAT-France campaign in spring 2008 between continental Norway and Svalbard. The instrument recorded scattered skylight spectra at the horizon, in which NO_2 and O_4 absorption structures were identified. The latter were used to infer aerosol extinction profiles at 360 nm, which were included in the NO_2 profile retrievals. The results were then interpreted using ancillary in situ chemical measurements and transport models back-trajectories.

For a sounding performed on 8 April 2008, the retrieved extinction is $0.04 \pm 0.005\,km^{-1}$ in the boundary layer and a smaller extinction layer ($0.01 \pm 0.003\,km^{-1}$) appears at 4 km altitude. NO_2 is also present in the boundary layer, its retrieved concentration being $1.9 \pm 0.3 \times 10^9$ molec cm^{-3}. For a sounding performed on the 9 April 2009, a layer with enhanced extinction and NO_2 was detected at 4 km altitude, with respective values of $0.025 \pm 0.005\,km^{-1}$ and $1.95 \pm 0.2 \times 10^9$ molec cm^{-3}.

For both soundings, the free troposphere extinction matched a layer with enhanced CO, indicating pollution transport, with rather different absolute values however. The small extinction detected in the first sounding is explained from back-trajectories as a mix between stratospheric and polluted air from Northwestern Europe, while the higher extinction seen the next day originated mostly from central Europe. The aerosols and NO_2 seen in the boundary layer during the first flight seem to originate from metal smelters and industry near Nikel on the Kola peninsula. The NO_2 layer at 4 km altitude

ACPD
11, 13525–13574, 2011

observed during the second flight seems to have been directly transported from central Europe with the CO and aerosols.

The instrument and the inversion method successfully fulfilled the scientific objectives of the study, yielding quantitative insights in the chemical composition and aerosol content of the Arctic troposphere, with a vertical resolution unachievable from ground or satellite, especially in the free troposphere. The logarithmic approach used for the aerosol extinction, which yielded better agreement with ancillary data in the two studied cases, should be further investigated as it also could improve ground-based retrievals. The experiment could be repeated in other areas to measure profiles of potentially all species detectable with the DOAS technique in our spectrometer spectral range. The high sensitivity could be further increased by adding a feedback on the scanning telescope to maintain it parallel to the horizon. We think interesting future applications can concern molecules for which fewer observations are available, such as IO which deserves further investigations due to its importance in ozone chemistry.

Acknowledgements. This work was supported by the Belgian Federal Science Policy (contract MO/35/028). POLARCAT-France was funded by French ANR, CNES, CNRS-INSU (LEFECHAT), IPEV and EUFAR, the latter funded also our participation to the campaign and a couple of additional hours. We are grateful to the UMS SAFIRE for their support in the instrument installation and providing the aircraft data. We also thank colleagues Corinne Vigouroux, François Hendrick, Emmanuel Dekemper, Valentin Duflot and Filip Vanhellemont for interesting discussions on the data analysis.

References

Ancellet, G., Leclair de Bellevue, J., Mari, C., Nedelec, P., Kukui, A., Borbon, A., and Perros, P.: Effects of regional-scale and convective transports on tropospheric ozone chemistry revealed by aircraft observations during the wet season of the AMMA campaign, Atmos. Chem. Phys., 9, 383–411, doi:10.5194/acp-9-383-2009, 2009. 13530, 13543

Beine, H. J. and Krognes, T.: The seasonal cycle of peroxyacetyl nitrate (PAN) in the European Arctic, Atmos. Environ., 34, 933–940, doi:10.1016/S1352-2310(99)00288-5, 2000. 13548

ACPD

11, 13525–13574, 2011

Boersma, K. F., Eskes, H. J., Veefkind, J. P., Brinksma, E. J., van der A, R. J., Sneep, M., van den Oord, G. H. J., Levelt, P. F., Stammes, P., Gleason, J. F., and Bucsela, E. J.: Near-real time retrieval of tropospheric NO_2 from OMI, Atmos. Chem. Phys., 7, 2103–2118, doi:10.5194/acp-7-2103-2007, 2007. 13533

Bogumil, K., Orphal, J., Homann, T., Voigt, S., Spietz, P., Fleischmann, O., Vogel, A., Hartmann, M., Kromminga, H., Bovensmann, H., Frerick, J., and Burrows, J.: Measurements of molecular absorption spectra with the SCIAMACHY pre-flight model: instrument characterization and reference data for atmospheric remote-sensing in the 230–2380 nm region, J. Photoch. Photobio. A., 157, 167–184, 2003. 13558

Bond, T. C., Habib, G., and Bergstrom, R. W.: Limitations in the enhancement of visible light absorption due to mixing state, J. Geophys. Res., 111, D20211, doi:10.1029/2006JD007315, 2006. 13544

Brandt, R. E., Warren, S. G., Worby, A. P., and Grenfell, T. C.: Surface Albedo of the Antarctic Sea Ice Zone, J. Climate, 18, 3606–3622, doi:10.1175/JCLI3489.1, 2005. 13533

Bruns, M., Buehler, S. A., Burrows, J. P., Richter, A., Rozanov, A., Wang, P., Heue, K. P., Platt, U., Pundt, I., and Wagner, T.: NO_2 Profile retrieval using airborne multi axis UV-visible skylight absorption measurements over central Europe, Atmos. Chem. Phys., 6, 3049–3058, doi:10.5194/acp-6-3049-2006, 2006. 13528

Chance, K. V. and Spurr, R. J. D.: Ring effect studies: Rayleigh scattering, including molecular parameters for rotational Raman scattering, and the Fraunhofer spectrum, Appl. Optics, 36, 5224–5230, doi:10.1364/AO.36.005224, 1997. 13532, 13558

Clémer, K., Van Roozendael, M., Fayt, C., Hendrick, F., Hermans, C., Pinardi, G., Spurr, R., Wang, P., and De Mazière, M.: Multiple wavelength retrieval of tropospheric aerosol optical properties from MAXDOAS measurements in Beijing, Atmos. Meas. Tech., 3, 863–878, doi:10.5194/amt-3-863-2010, 2010. 13527

de Villiers, R. A., Ancellet, G., Pelon, J., Quennehen, B., Schwarzenboeck, A., Gayet, J. F., and Law, K. S.: Airborne measurements of aerosol optical properties related to early spring transport of mid-latitude sources into the Arctic, Atmos. Chem. Phys., 10, 5011–5030, doi:10.5194/acp-10-5011-2010, 2010. 13530, 13546

Deeter, M. N., Edwards, D. P., and Gille, J. C.: Retrievals of carbon monoxide profiles from MOPITT observations using lognormal a priori statistics, J. Geophys. Res., 112, D11311, doi:10.1029/2006JD007999, 2007. 13537

Dils, B.: Long Range Transport of Tropospheric NO2 as simulated by FLEXPART, Product

ACPD
11, 13525–13574, 2011

Specification Document TEM/LRT2/001, TEMIS, De Bilt, The Netherlands, 2008. 13548
Dubovik, O. V., Lapyonok, T. V., and Oshchepkov, S. L.: Improved technique for data inversion: optical sizing of multicomponent aerosols, Appl. Optics, 34, 8422–8436, doi:10.1364/AO.34.008422, 1995. 13545
Forster, C., Wandinger, U., Wotawa, G., James, P., Mattis, I., Althausen, D., Simmonds, P., O'Doherty, S., Jennings, S. G., Kleefeld, C., Schneider, J., Trickl, T., Kreipl, S., Jäger, H., and Stohl, A.: Transport of boreal forest fire emissions from Canada to Europe, J. Geophys. Res., 106, 22887–22906, doi:10.1029/2001JD900115, 2001. 13546
Friess, U., Monks, P. S., Remedios, J. J., Rozanov, A., Sinreich, R., Wagner, T., and Platt, U.: MAX-DOAS O_4 measurements: A new technique to derive information on atmospheric aerosols: 2. Modeling studies, J. Geophys. Res., 111, D14203, doi:10.1029/2005JD006618, 2006. 13527
Grainger, J. F. and Ring, J.: Anomalous Fraunhofer Line Profiles, Nature, 193(4817), 762 pp., doi:10.1038/193762a0, 1962. 13532
Granier, C., Niemeier, U., Jungclaus, J. H., Emmons, L., Hess, P., Lamarque, J., Walters, S., and Brasseur, G. P.: Ozone pollution from future ship traffic in the Arctic northern passages, Geophys. Res. Lett., 33, L13807, doi:10.1029/2006GL026180, 2006. 13527
Harder, J. W. and Brault, J. W.: Atmospheric measurements of water vapor in the 442-nm region, J. Geophys. Res., 102, 6245–6252, doi:10.1029/96JD01730, 1997. 13558
Hendrick, F., Van Roozendael, M., Kylling, A., Petritoli, A., Rozanov, A., Sanghavi, S., Schofield, R., von Friedeburg, C., Wagner, T., Wittrock, F., Fonteyn, D., and De Mazière, M.: Intercomparison exercise between different radiative transfer models used for the interpretation of ground-based zenith-sky and multi-axis DOAS observations, Atmos. Chem. Phys., 6, 93–108, doi:10.5194/acp-6-93-2006, 2006. 13537
Herber, A., Thomason, L. W., Gernandt, H., Leiterer, U., Nagel, D., Schulz, K., Kaptur, J., Albrecht, T., and Notholt, J.: Continuous day and night aerosol optical depth observations in the Arctic between 1991 and 1999, J. Geophys. Res., 107, 4097, doi:10.1029/2001JD000536, 2002. 13538
Hess, M., Koepke, P., and Schult, I.: Optical Properties of Aerosols and Clouds: The Software Package OPAC, B. Am. Meteorol. Soc., 79, 831–844, 1998. 13536
Hönninger, G., von Friedeburg, C., and Platt, U.: Multi axis differential optical absorption spectroscopy (MAX-DOAS), Atmos. Chem. Phys., 4, 231–254, doi:10.5194/acp-4-231-2004, 2004. 13527, 13529

ACPD
11, 13525–13574, 2011

Honrath, R. E., Peterson, M. C., Guo, S., Dibb, J. E., Shepson, P. B., and Campbell, B.: Evidence of NOx production within or upon ice particles in the Greenland snowpack, Geophys. Res. Lett., 26, 695–698, doi:10.1029/1999GL900077, 1999. 13548

Irie, H., Kanaya, Y., Akimoto, H., Iwabuchi, H., Shimizu, A., and Aoki, K.: First retrieval of tropospheric aerosol profiles using MAX-DOAS and comparison with lidar and sky radiometer measurements, Atmos. Chem. Phys., 8, 341–350, doi:10.5194/acp-8-341-2008, 2008. 13527

Law, K. and Stohl, A.: Arctic Air Pollution: Origins and Impacts, Science, 315, 1537–1540, doi:10.1126/science.1137695, 2007. 13527

Levelt, P., van den Oord, G., Dobber, M., Malkki, A., Visser, H., de Vries, J., Stammes, P., Lundell, J., and Saari, H.: The ozone monitoring instrument, IEEE T. Geosci. Remote., 44, 1093–1101, doi:10.1109/TGRS.2006.872333, 2006. 13528

Matzler, C.: Matlab functions for Mie scattering and absorption, Research report no. 2002-08, Institut für Angewandte Physik, Bern, 2002. 13544

Mayer, B. and Kylling, A.: Technical note: The libRadtran software package for radiative transfer calculations – description and examples of use, Atmos. Chem. Phys., 5, 1855–1877, doi:10.5194/acpd-5-1319-2005, 2005. 13533

McPeters, R. D., Labow, G. J., and Logan, J. A.: Ozone climatological profiles for satellite retrieval algorithms, J. Geophys. Res., 112, D05308, doi:10.1029/2005JD006823, 2007. 13533

Nedelec, P., Cammas, J.-P., Thouret, V., Athier, G., Cousin, J.-M., Legrand, C., Abonnel, C., Lecoeur, F., Cayez, G., and Marizy, C.: An improved infrared carbon monoxide analyser for routine measurements aboard commercial Airbus aircraft: technical validation and first scientific results of the MOZAIC III programme, Atmos. Chem. Phys., 3, 1551–1564, doi:10.5194/acp-3-1551-2003, 2003. 13530

Olivier, J., Aardenne, J. V., Dentener, F., Pagliari, V., Ganzeveld, L., and Peters, J.: Recent trends in global greenhouse gas emissions: regional trends 1970–2000 and spatial distribution of key sources in 2000, Env. Sc., 2, 81–99, doi:10.1080/15693430500400345, 2005. 13549

Platt, U. and Stutz, J.: Differential Optical Absorption Spectroscopy: Principles and Applications, Physics of Earth and Space Environments, Springer, Berlin, 2008. 13527, 13531

Prados-Roman, C., Butz, A., Deutschmann, T., Dorf, M., Kritten, L., Minikin, A., Platt, U., Schlager, H., Sihler, H., Theys, N., Van Roozendael, M., Wagner, T., and Pfeilsticker, K.: Airborne DOAS limb measurements of tropospheric trace gas profiles: case study on the profile

ACPD
11, 13525–13574, 2011

retrieval of O_4 and BrO, Atmos. Meas. Tech. Discuss., 3, 3925–3969, doi:10.5194/amtd-3-3925-2010, 2010. 13528, 13538

Prank, M., Sofiev, M., van der Gon, H. A. C. D., Kaasik, M., Ruuskanen, T. M., and Kukkonen, J.: A refinement of the emission data for Kola Peninsula based on inverse dispersion modelling, Atmos. Chem. Phys., 10, 10849–10865, doi:10.5194/acp-10-10849-2010, 2010. 13549, 13550

Ridley, B., Walega, J., Montzka, D., Grahek, F., Atlas, E., Flocke, F., Stroud, V., Deary, J., Gallant, A., Boudries, H., Bottenheim, J., Anlauf, K., Worthy, D., Sumner, A. L., Splawn, B., and Shepson, P.: Is the Arctic Surface Layer a Source and Sink of NO_x in Winter/Spring?, J. Atmos. Chem., 36, 1–22, doi:10.1023/A:1006301029874, 2000. 13543

Rodgers, C. D.: Inverse Methods for Atmospheric Sounding : Theory and Practice, World Scientific Publishing Company, 2000. 13531, 13535, 13536

Schneider, M., Hase, F., and Blumenstock, T.: Water vapour profiles by ground-based FTIR spectroscopy: study for an optimised retrieval and its validation, Atmos. Chem. Phys., 6, 811–830, doi:10.5194/acp-6-811-2006, 2006. 13537, 13545

Shaw, G. E.: The Arctic Haze Phenomenon, B. Am. Meteorol. Soc., 76, 2403–2414, doi:10.1175/1520-0477(1995)076¡2403:TAHP¿2.0.CO;2, 1995. 13527

Stohl, A., Forster, C., Eckhardt, S., Spichtinger, N., Huntrieser, H., Heland, J., Schlager, H., Wilhelm, S., Arnold, F., and Cooper, O.: A backward modeling study of intercontinental pollution transport using aircraft measurements, J. Geophys. Res., 108, 4370, doi:10.1029/2002JD002862, 2003. 13548

Stohl, A., Forster, C., Frank, A., Seibert, P., and Wotawa, G.: Technical note: The Lagrangian particle dispersion model FLEXPART version 6.2, Atmos. Chem. Phys., 5, 2461–2474, doi:10.5194/acp-5-2461-2005, 2005. 13548

Stohl, A., Forster, C., Huntrieser, H., Mannstein, H., McMillan, W. W., Petzold, A., Schlager, H., and Weinzierl, B.: Aircraft measurements over Europe of an air pollution plume from Southeast Asia – aerosol and chemical characterization, Atmos. Chem. Phys., 7, 913–937, doi:10.5194/acp-7-913-2007, 2007. 13547

Stroud, C., Madronich, S., Atlas, E., Ridley, B., Flocke, F., Weinheimer, A., Talbot, B., Fried, A., Wert, B., Shetter, R., Lefer, B., Coffey, M., Heikes, B., and D., B.: Photochemistry in the arctic free troposphere: NO_x budget and the role of odd nitrogen reservoir recycling, Atmos. Environ., 37, 3351–3364, doi:10.1016/S1352-2310(03)00353-4, 2003. 13539, 13548

Tomasi, C., Vitale, V., Lupi, A., Carmine, C. D., Campanelli, M., Herber, A., Treffeisen, R.,

ACPD
11, 13525–13574, 2011

Stone, R. S., Andrews, E., Sharma, S., Radionov, V., von Hoyningen-Huene, W., Stebel, K., Hansen, G. H., Myhre, C. L., Wehrli, C., Aaltonen, V., Lihavainen, H., Virkkula, A., Hillamo, R., Ström, J., Toledano, C., Cachorro, V. E., Ortiz, P., de Frutos, A. M., Blindheim, S., Frioud, M., Gausa, M., Zielinski, T., Petelski, T., and Yamanouchi, T.: Aerosols in polar regions: A historical overview based on optical depth and in situ observations, J. Geophys. Res., 112, D16205, doi:10.1029/2007JD008432, 2007. 13544

Vanhellemont, F., Fussen, D., Mateshvili, N., Tétard, C., Bingen, C., Dekemper, E., Loodts, N., Kyrölä, E., Sofieva, V., Tamminen, J., Hauchecorne, A., Bertaux, J.-L., Dalaudier, F., Blanot, L., Fanton d'Andon, O., Barrot, G., Guirlet, M., Fehr, T., and Saavedra, L.: Optical extinction by upper tropospheric/stratospheric aerosols and clouds: GOMOS observations for the period 20022008, Atmos. Chem. Phys., 10, 7997–8009, doi:10.5194/acp-10-7997-2010, 2010. 13547

Villani, P., Picard, D., Michaud, V., Laj, P., and Wiedensohler, A.: Design and Validation of a Volatility Hygroscopic Tandem Differential Mobility Analyzer (VH-TDMA) to Characterize the Relationships Between the Thermal and Hygroscopic Properties of Atmospheric Aerosol Particles, Aerosol. Sci. Tech., 42, 729–741, doi:10.1080/02786820802255668, 2008. 13530

Wagner, T., Dix, B., Friedeburg, C. V., Friess, U., Sanghavi, S., Sinreich, R., and Platt, U.: MAX-DOAS O4 measurements: A new technique to derive information on atmospheric aerosols: 1. Principles and information content, J. Geophys. Res., 109, D22205, doi:10.1029/2004JD004904, 2004. 13527

Wagner, T., Burrows, J. P., Deutschmann, T., Dix, B., von Friedeburg, C., Frieß, U., Hendrick, F., Heue, K.-P., Irie, H., Iwabuchi, H., Kanaya, Y., Keller, J., McLinden, C. A., Oetjen, H., Palazzi, E., Petritoli, A., Platt, U., Postylyakov, O., Pukite, J., Richter, A., van Roozendael, M., Rozanov, A., Rozanov, V., Sinreich, R., Sanghavi, S., and Wittrock, F.: Comparison of box-air-mass-factors and radiances for Multiple-Axis Differential Optical Absorption Spectroscopy (MAX-DOAS) geometries calculated from different UV/visible radiative transfer models, Atmos. Chem. Phys., 7, 1809–1833, doi:10.5194/acp-7-1809-2007, 2007. 13534

Wittrock, F., Oetjen, H., Richter, A., Fietkau, S., Medeke, T., Rozanov, A., and Burrows, J. P.: MAX-DOAS measurements of atmospheric trace gases in Ny-Å lesund – Radiative transfer studies and their application, Atmos. Chem. Phys., 4, 955–966, doi:10.5194/acp-4-955-2004, 2004. 13527, 13535, 13543, 13548

Zahn, A., Brenninkmeijer, C. A. M., Maiss, M., Scharffe, D. H., Crutzen, P. J., Hermann, M., Heintzenberg, J., Wiedensohler, A., Gãsten, H., Heinrich, G., Fischer, H., Cuijpers, J. W. M.,

ACPD
11, 13525–13574, 2011

and van Velthoven, P. F. J.: Identification of extratropical two-way troposphere-stratosphere mixing based on CARIBIC measurements of O_3, CO, and ultrafine particles, J. Geophys. Res., 105, 1527–1535, doi:10.1029/1999JD900759, 2000. 13547

Zhou, Y., Brunner, D., Boersma, K. F., Dirksen, R., and Wang, P.: An improved tropospheric NO_2 retrieval for OMI observations in the vicinity of mountainous terrain, Atmos. Meas. Tech., 2, 401–416, doi:10.5194/amt-2-401-2009, 2009. 13534, 13535

Zieger, P., Weingartner, E., Henzing, J., Moerman, M., de Leeuw, G., Mikkilä, J., Ehn, M., Petäjä, T., Clémer, K., van Roozendael, M., Yilmaz, S., Frieß, U., Irie, H., Wagner, T., Shaiganfar, R., Beirle, S., Apituley, A., Wilson, K., and Baltensperger, U.: Comparison of ambient aerosol extinction coefficients obtained from in-situ, MAX-DOAS and LIDAR measurements at Cabauw, Atmos. Chem. Phys. Discuss., 10, 29683–29734, doi:10.5194/acpd-10-29683-2010, 2010. 13540, 13541

ACPD
11, 13525–13574, 2011

Table 1. DOAS analysis settings.

	O_4	NO_2
Fitting window	340–370 nm	428–450 nm
O_4	Hermans (see text)	Ibid.
NO_2	Bogumil et al. (2003)	Ibid.
O_3	Bogumil et al. (2003)	Ibid.
H_2O	–	Harder and Brault (1997)
Ring	Chance and Spurr (1997)	Ibid.
Polynomial order	3	5

ACPD
11, 13525–13574, 2011

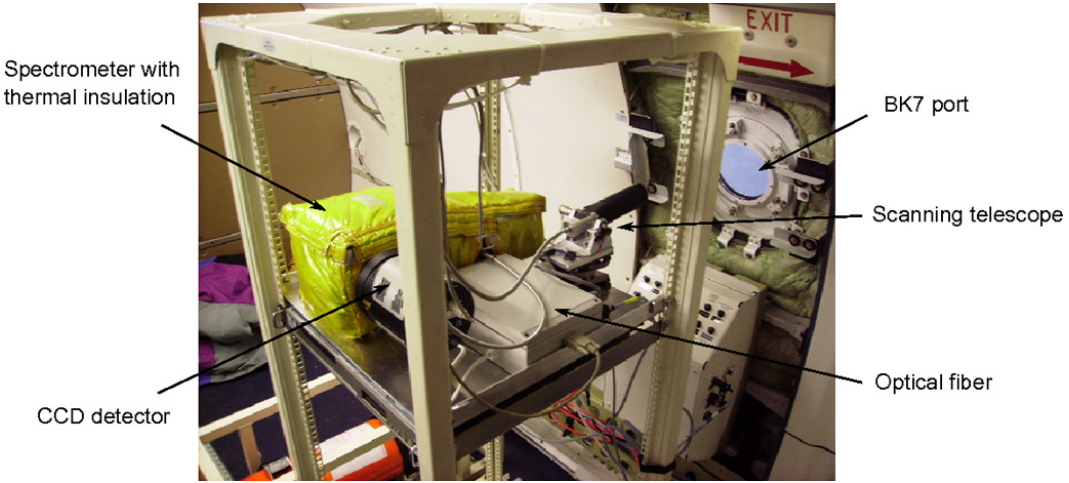

Fig. 1. The Airborne Limb Scanning Differential Optical Absorption Spectrometer (ALS-DOAS) onboard the Safire ATR-42 aircraft. A scanning telescope collects scattered sky-light at different angles near the horizon, this light being transmitted through an optical fiber to a grating spectrometer. A CCD detector is used to record the spectra. See text for technical details.

ACPD
11, 13525–13574, 2011

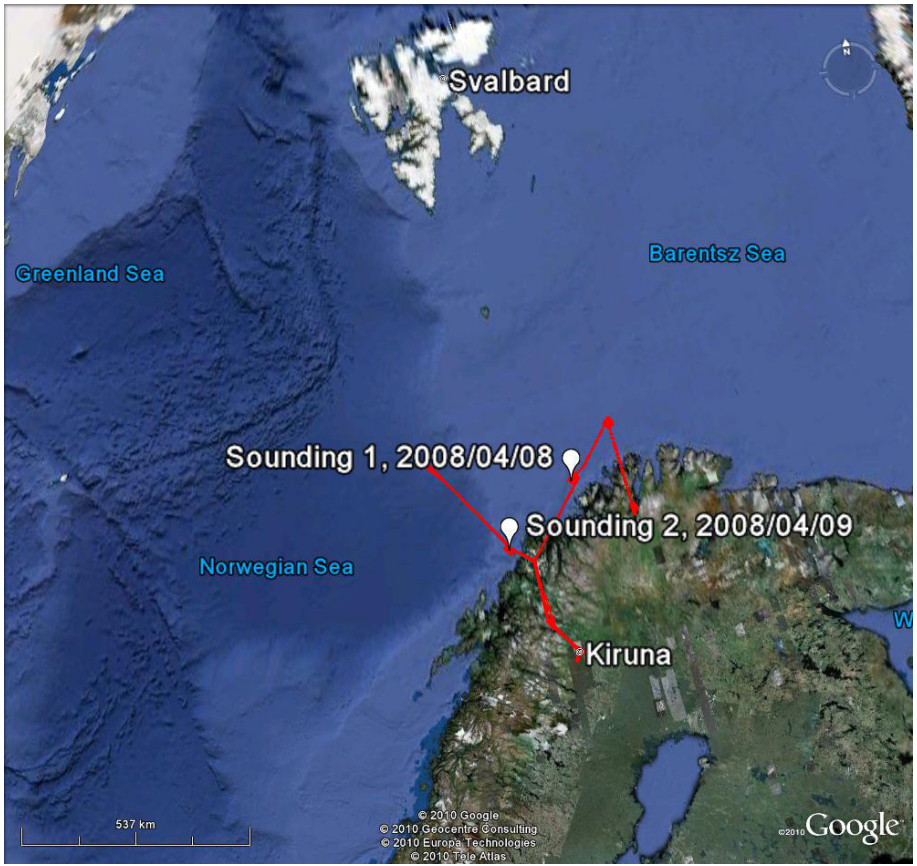

Fig. 2. Tracks of the flights as0831 (8 April 2008) and as0833 (9 April 2008) of the POLARCAT-FRANCE Spring campaign. Two soundings are studied in this work, respectively at 71° N, 22° E and 70° N, 17.8° E.

ACPD
11, 13525–13574, 2011

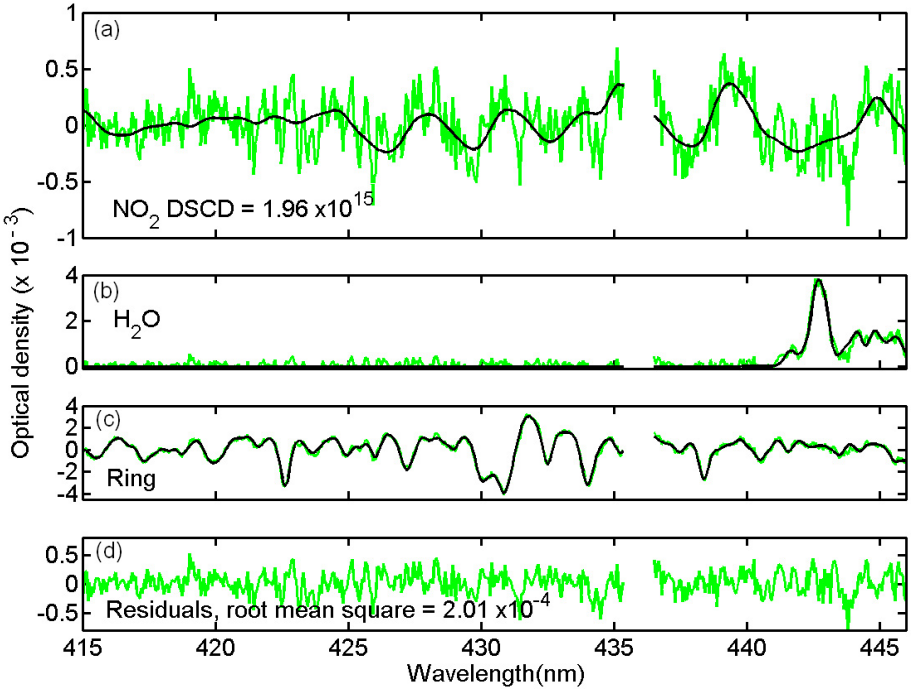

Fig. 3. Example of a DOAS fit. Black lines correspond to molecular and Ring cross-sections scaled to the detected absorptions in the measured spectrum (green lines). Note that the pixels between 435.4 and 436.5 nm are damaged.

ACPD
11, 13525–13574, 2011

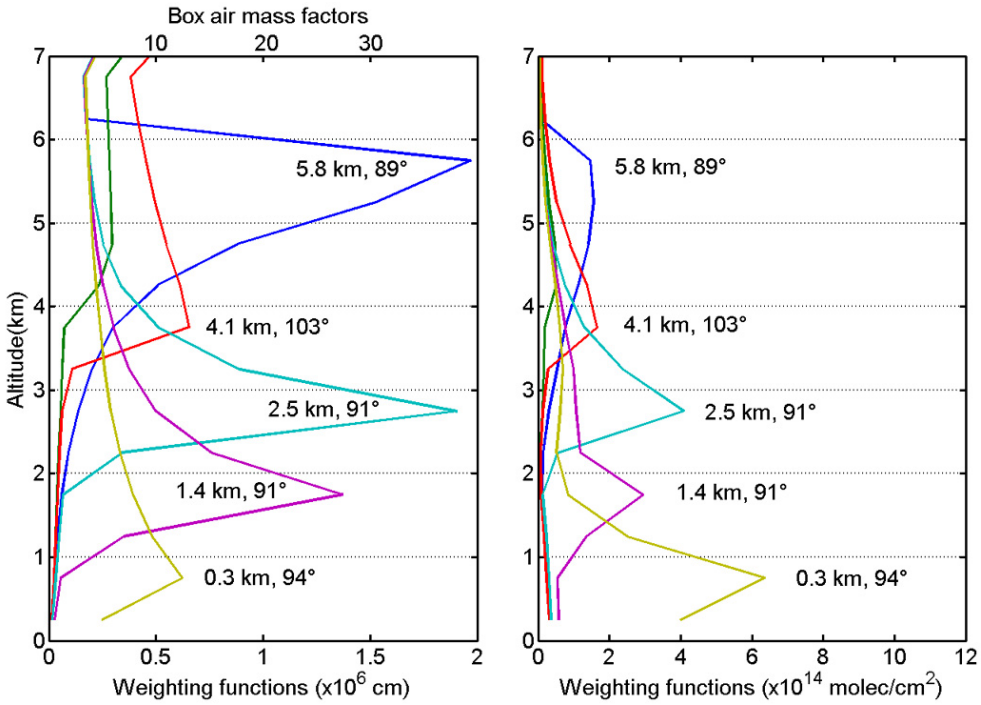

Fig. 4. Some of the weighting functions relative to the NO_2 slant column measurements of the 8 April 2008 in linear (left panel) and logarithmic (right panel) scale. Beside the altitudes of observations are indicated the telescope line-of-sight angles (0° is nadir, 90° horizontal).

ACPD
11, 13525–13574, 2011

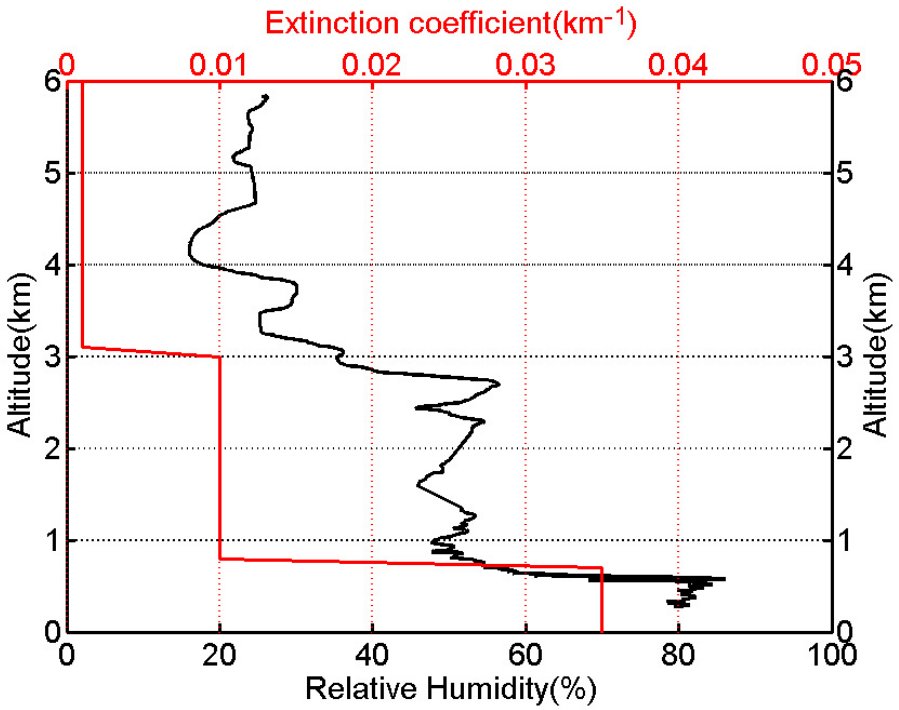

Fig. 5. Construction of the a priori aerosol extinction coefficient profile (red) from the measured relative humidity (black). The extinction values are derived from the software package OPAC, using the Arctic Spring predefined aerosol type.

ACPD
11, 13525–13574, 2011

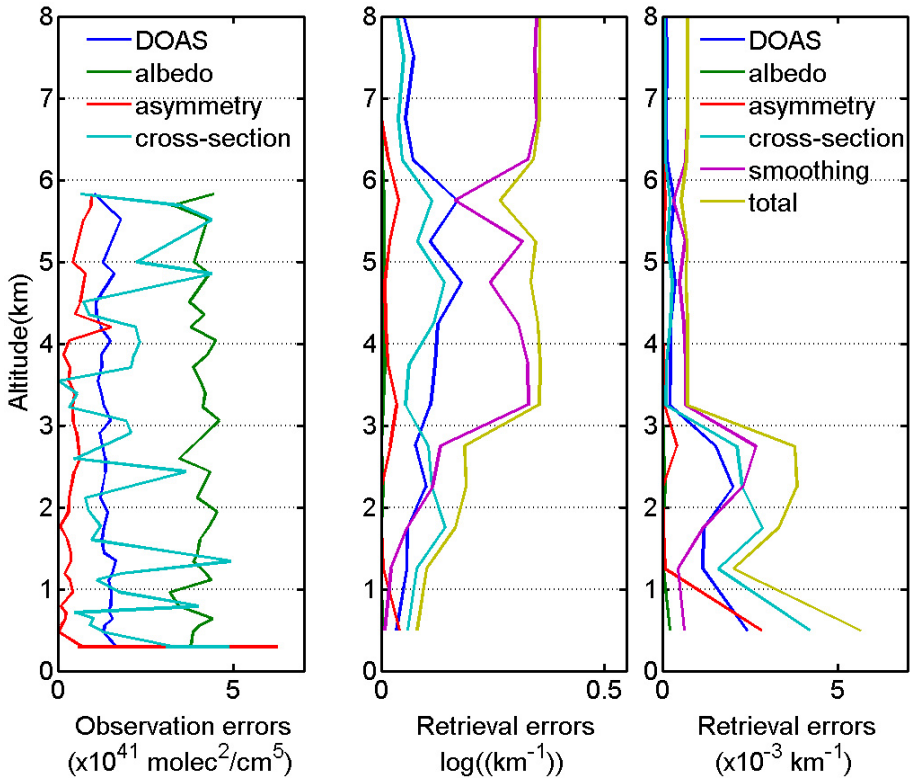

Fig. 6. Error contributions for the extinction profile of the 8 April 2008 retrieved in logarithmic scale, estimated from the diagonal elements of the error covariance matrices.

ACPD
11, 13525–13574, 2011

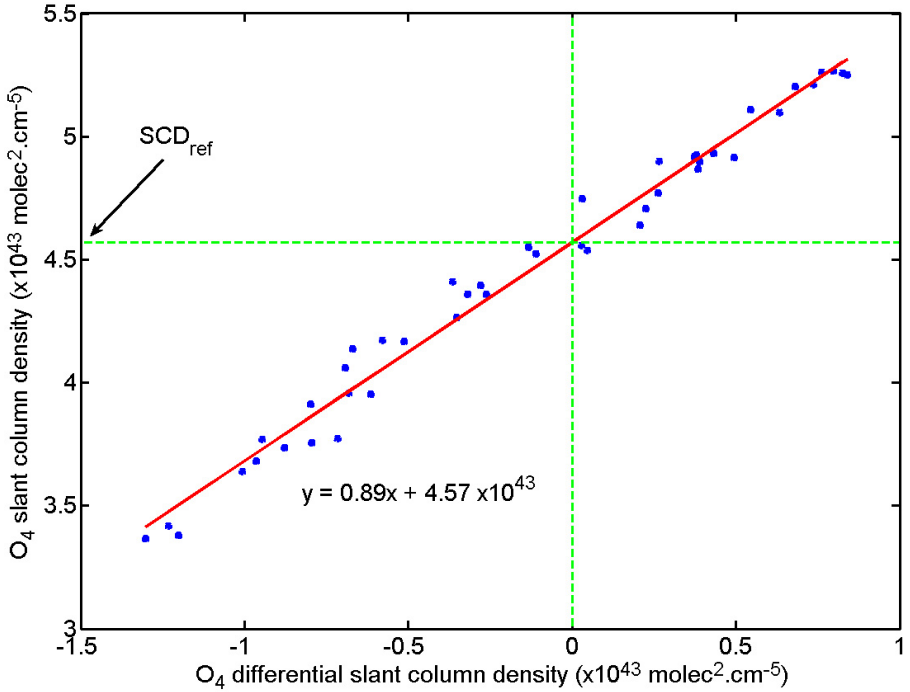

Fig. 7. Determination of the residual column density and of the O_4 cross-section correcting factor. DSCD measurements at high altitude, where aerosols scattering can be neglected, are plotted versus simulated absolute SCD. The linear regression fits simultaneously the residual slant column density in the reference spectrum (the intercept, SCD_{ref}) and the cross-section correcting factor (inverse of the slope).

ACPD
11, 13525–13574, 2011

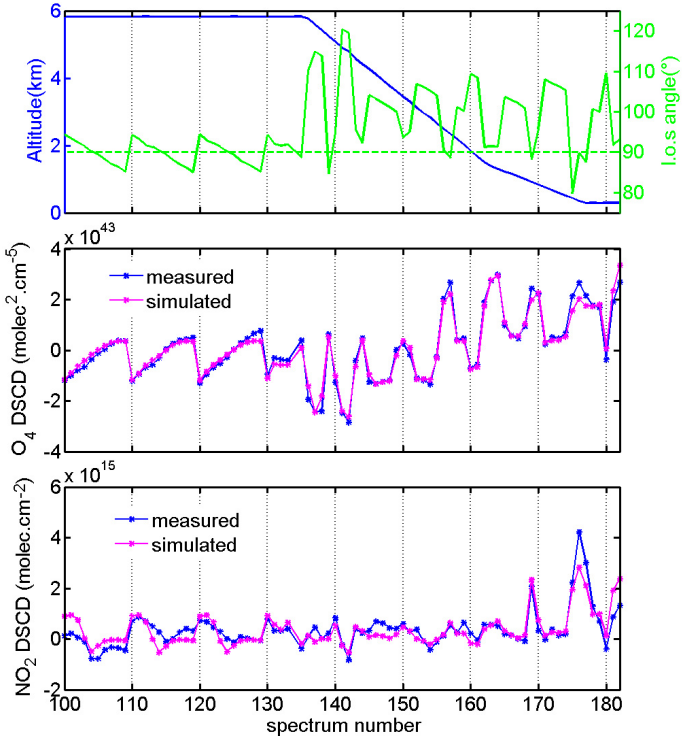

Fig. 8. DSCD measurements during the as0831 flight (8 April 2008). The upper panel shows the plane altitude (blue) and the telescope line-of-sight angle (green, 0° is nadir, 90° horizontal). On the middle and bottom panels, measured DSCD, respectively of O_4 and NO_2, are compared with simulations. Oscillations on the DSCD series are caused by the telescope scanning. Discrepancies between measured and simulated DSCD are larger in the boundary layer, where true aerosol extinction and NO_2 concentration are different from the model.

ACPD
11, 13525–13574, 2011

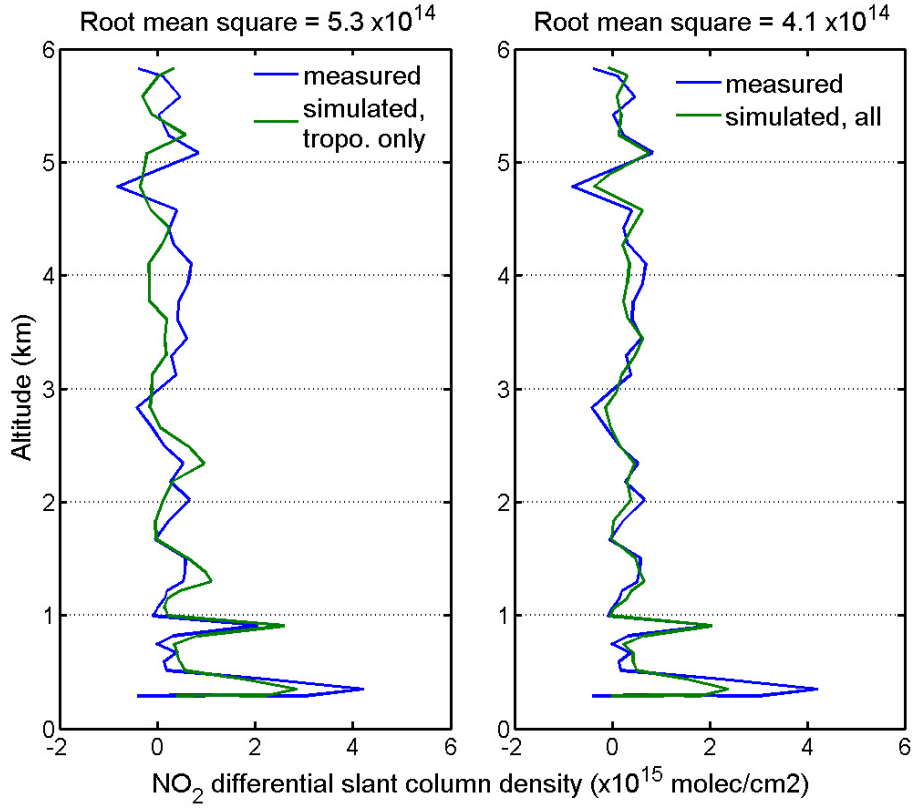

Fig. 9. Influence of the stratosphere on NO_2 tropospheric observations. Measured NO_2 DSCD during the sounding (blue) are compared with simulations (green) neglecting the stratosphere (left) or not (right). The latter agrees better with the observations.

ACPD
11, 13525–13574, 2011

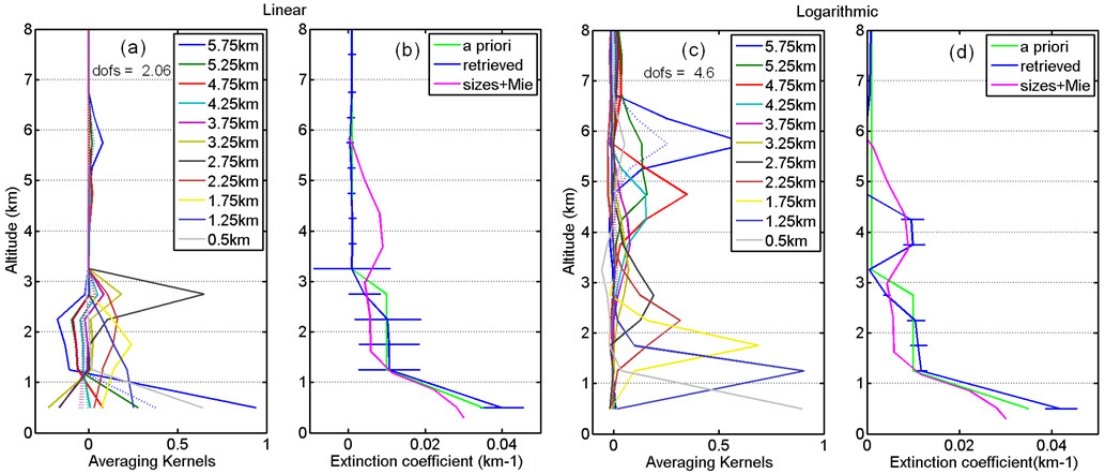

Fig. 10. Comparison of the aerosol extinction profile retrieval in linear and logarithmic scale for the sounding of the as0831 flight (8 April 2008). For the same a priori, the logarithmic retrieval agrees better with an extinction profile calculated from in situ size distribution. Averaging kernels indicate also a higher sensitivity of the retrieval to the true state in the logarithmic case.

ACPD
11, 13525–13574, 2011

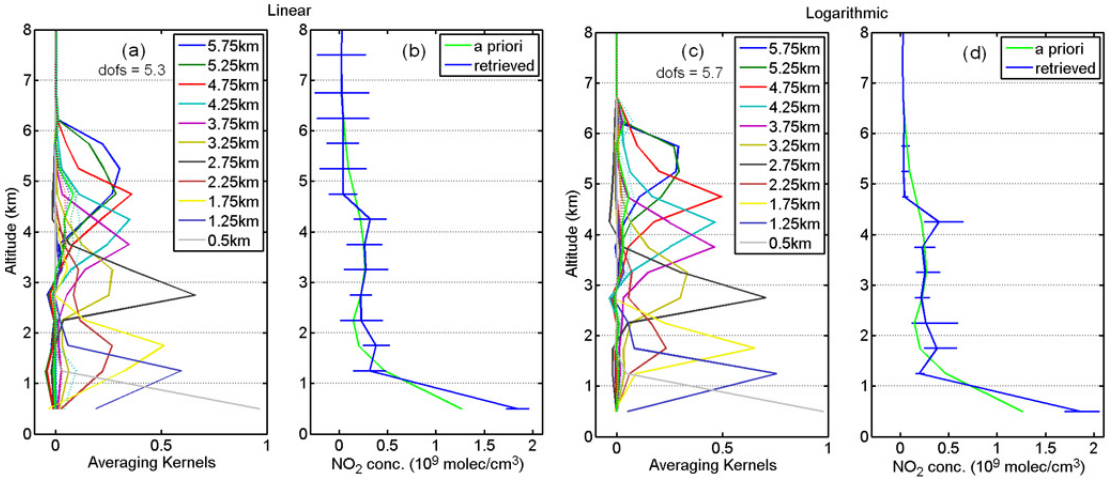

Fig. 11. Comparison of the retrieved NO_2 profile for the sounding of the as0831 flight (8 April 2008), with the two optimal estimation strategies, normal (left) and lognormal a priori (right). The two panels show the respective weighting functions, averaging kernels, and retrieved profiles. The results are very close, contrary to the aerosol extinction retrieval.

ACPD
11, 13525–13574, 2011

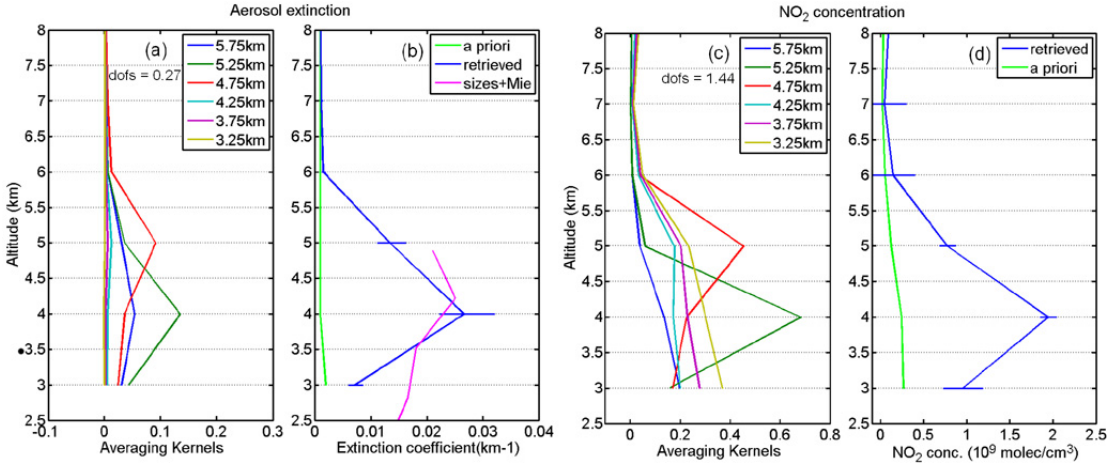

Fig. 12. Retrieved extinction and NO_2 profiles for the sounding of the as0833 flight (9 April 2008). Under 3 km high, the radiative transfer is too much affected by clouds to enable quantitative retrievals. Around 4 km high, an enhanced layer is measured for both extinction and NO_2.

ACPD
11, 13525–13574, 2011

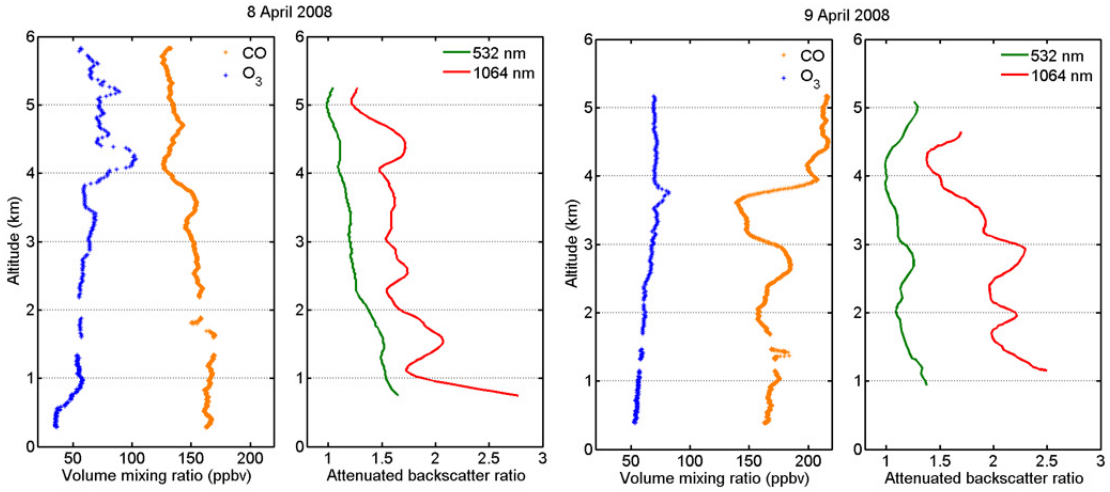

Fig. 13. Ozone and CO in situ measurements during the two soundings studied in this work. On the second one (9 April 2008) a layer with enhanced CO above 3.7 km indicates pollution transport.

ACPD
11, 13525–13574, 2011

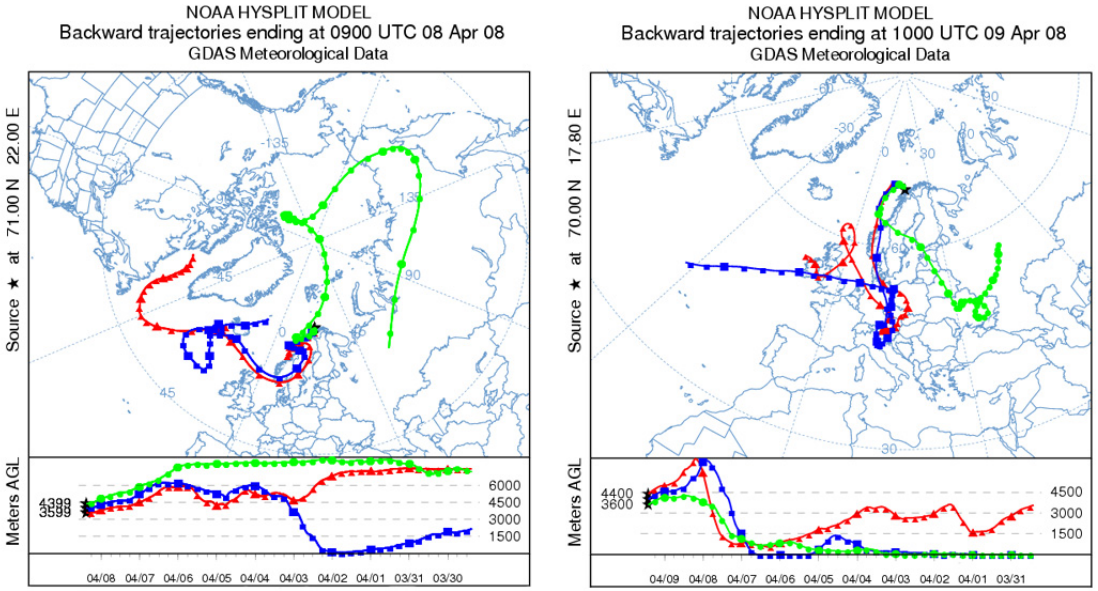

Fig. 14. Back-trajectories for the two soundings positions calculated for altitudes of 3.6, 4 and 4.4 km. During flight as0833 (9 April 2008), the air masses are clearly influenced by polluted zones, i.e. the boundary layer in central Europe.

ACPD
11, 13525–13574, 2011

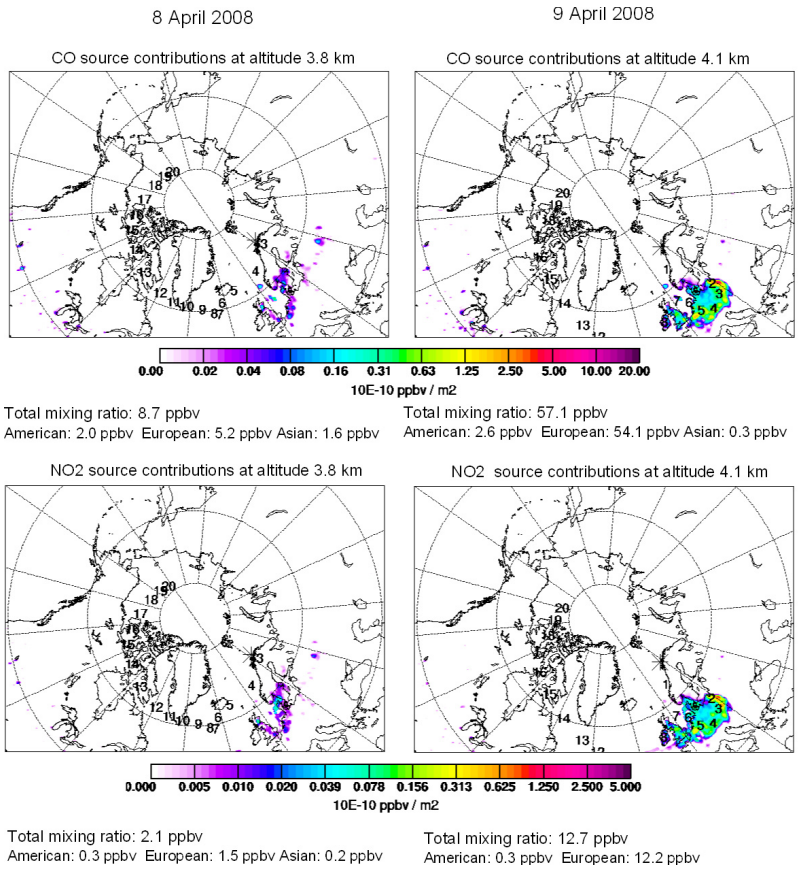

Fig. 15. CO and NO_2 source contributions for the altitude with maximum CO concentration in the two soundings. Europe appears the dominant source and its influence is much larger on the second sounding (9 April 2008).

ACPD
11, 13525–13574, 2011

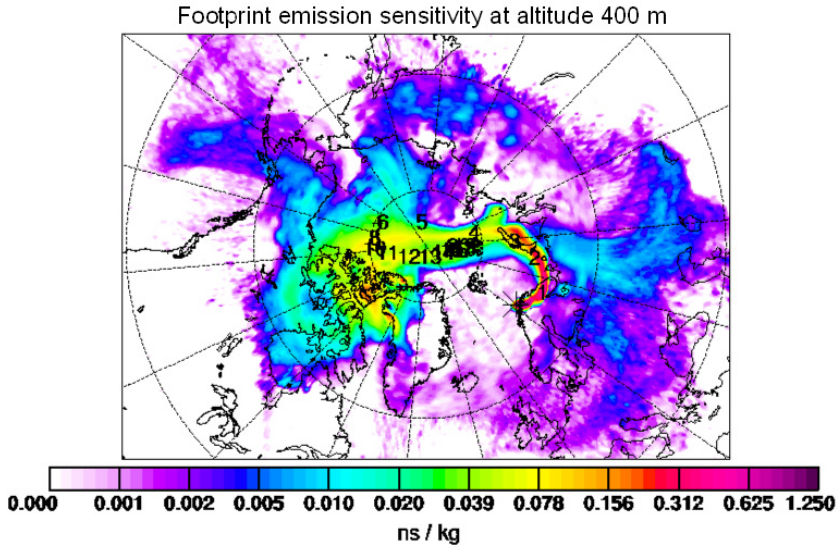

Fig. 16. Footprint emission sensitivity for the air in the boundary layer of the 8 April 2008 sounding, where enhanced NO_2 is measured.

ACPD
11, 13525–13574, 2011